DIFFUSION WEIGHTED MAGNETIC RESONANCE IMAGING BY TEMPORAL DIFFUSION SPECTROSCOPY

By

Junzhong Xu

Dissertation

Submitted to the Faculty of the

Graduate School of Vanderbilt University

in partial fulfillment of the requirements

for the degree of

DOCTOR OF PHILOSOPHY

in

Physics

December 2008

Nashville, Tennessee

Approved by

Professor John C. Gore

Professor Mark D. Does

Professor Adam W. Anderson

Professor Vito Quaranta

Professor Alan R. Tackett

ACKNOWLEDGEMENT

This dissertation would never have been possible without the consistent vision, steady example and patient encouragement of my adviser, Prof. John Gore. It has been really lucky to work under his supervision. I greatly appreciate Prof. Mark Does for his inspiring discussions and continuous directions during my graduate study. I would like to thank Prof. Adam Anderson, Prof. Vito Quaranta and Prof. Alan Tackett for being on my committee and for their teaching, suggestions and criticism.

I would like to thank my current and former colleagues for their kind help and many motivating discussions, specifically to Drs. Ha-Kyu Jeong, Wilson Barros, Richard Baheza, Jeff Luci, Jingping Xie and Daniel Colvin.

I would like to express my appreciation to Vanderbilt University Department of Physics and Astronomy and Vanderbilt University Institute of Imaging Science for providing excellent education and establishing an environment of state-of-the-art imaging resources for our graduate students. My research was funded by NIH grants R01 CA109106 and R01 NS034834.

My family has been supportive throughout my education, encouraging my decisions and providing much needed love. Finally and firstly, this dissertation is dedicated to my wife Guozhen, whose love, hard work and patience have made my last six years a joy.

ABSTRACT

Diffusion-weighted magnetic resonance imaging (DWI) provides a unique approach for probing the microstructure of biological tissues and is an important tool for both clinical and research applications, such as for the diagnosis of stroke and detection of cancer. However, conventional DWI measurements using pulsed gradient spin echo (PGSE) methods cannot in practice probe very short diffusion times because of hardware limitations, and this restriction prevents conventional DWI from being able to characterize changes in intra-cellular structure, which may be critical in many applications. The method of diffusion temporal spectroscopy using oscillating gradient spin echo (OGSE) methods has been proposed to probe short diffusion times and to provide additional contrast in diffusion imaging. A comprehensive study of diffusion temporal spectroscopy is presented in this thesis, including (1) a simulation of OGSE methods in cellular systems using an improved finite difference method for more accurate and efficient computation of results ; (2) studies of biological tissues and DWI signals with diffusion temporal spectroscopy in order to predict and interpret data and extract quantitative tissue microstructural information; and (3) demonstration of the increased sensitivity of DWI measurements to variations of intracellular structures, such as nuclear sizes, using the diffusion temporal spectroscopy method. The work presented here provides a framework to interpret DWI data to obtain biological tissue microstructural information and may enhance the ability of diffusion imaging to be used as a biomarker for, for example, assessing the state of tumors in pre-clinical research.

TABLE OF CONTENTS

LIST OF FIGURES

Chapter V

LIST OF TABLES

CHAPTER I

INTRODUCTION

Magnetic resonance imaging (MRI) has been one of the most exciting and active modalities in medical imaging in the past 30 years. Seven outstanding scientists have been awarded Nobel Prizes for their major contributions to the discovery and development of NMR and MRI. Compared to other medical imaging modalities, MRI has a magnificent ability to differentiate soft tissues and provides an abundance of anatomical, physiological and functional information. MRI has become a major diagnostic tool in clinical practice, such as for the detection of tumors and strokes, and it is also a powerful tool for many research studies, such as studies of brain structure and function in neuroscience. Section 1.1 briefly goes over the history of NMR and MRI.

After the Brownian motion of particles was first described, it remained mysterious until Einstein explained it using statistical mechanics and kinetic theory. Since then, studies of diffusion have been of interest in many research areas and diffusion-weighted magnetic resonance imaging (DWI) has proven to be a powerful tool in clinical and research applications. Section 1.2 introduces a brief history of diffusion and DWI.

The basic concepts of NMR and MRI are discussed in Section 1.3 , including definitions of the Larmor frequency, T_1 and T_2 relaxation times, the Bloch equation and the formation of magnetic resonance images.

Section 1.4 introduces the basic principles of diffusion and DWI, including Brownian motion, Einstein's equation, the Bloch-Torrey equation, the pulsed gradient spin echo (PGSE) method and the q-space.

1.1 A Brief History of NMR and MRI

The concept of nuclear magnetic resonance originated from the work introduced by Rabi in 1938. He showed that electromagnetic waves with certain frequencies could flip magnetically aligned nuclei from one state to the other (given that for spin half nuclei there are two possible states: a

lower energy state and a higher energy state) (1). Hence, the magnetic properties of atomic nuclei can be obtained by a ‘resonance’ method, for which Rabi won the Nobel Prize in Physics in 1944. Eight years later, Bloch and Purcell refined the technique for use on liquids and solids. Purcell studied the precession of nuclear magnetization in a magnetic field with a fixed radiofrequency (RF) and observed a sharp absorption of radiation as nuclei flipped from the lower to the higher energy state, and he named this phenomenon ‘nuclear magnetic resonance’ (NMR) (2). Almost simultaneously, Bloch investigated the water in an adjustable magnetic field and, rather than measuring absorption, he detected re-emission of resonant radiation using a second coil placed perpendicular to the first (3). Although Rabi's work was crucial, both works by Purcell and Bloch were a very big leap forward, which laid the foundation for the development of modern NMR and MRI techniques, for which Bloch and Purcell shared the Nobel Prize in Physics in 1952. In 1950, Hahn discovered the spin echo (4), which is considered the beginning of the widespread use of pulsed NMR methods. Ernst developed the methodology of high resolution pulsed Fourier Transform nuclear magnetic resonance spectroscopy, for which he won the Nobel Prize in Chemistry in 1991. In 2002, Wüthrich won the Nobel Prize in Chemistry for his development of NMR spectroscopy for determining the three-dimensional structure of biological macromolecules in solution.

In 1973, Lauterbur published a paper in Nature, which described the use of linear magnetic field gradients to spatially localize NMR signals (5). He obtained spectra that were actually the projections of the object’s spin density distribution onto the gradient axis. By rotating the object in the field, a series of angular projections could be obtained and two-dimensional MR images can be reconstructed by using the mathematics of filtered back projection developed for computed tomography. Because it can be considered as an interaction of polarizing and gradient fields, Lauterbur named this methodology as “zeugmatography” (derived from the Greek word ζενγμα--“that which is used for joining”). Soon after that, Sir. Peter Mansfield published an extensive paper showing projection images of a human finger, which perhaps was the first MRI of live human anatomy (6). In order to speed up the scan acquisition, he also developed an MRI

protocol called echo planar imaging (EPI) (7), which makes fast imaging possible. Lauterbur and Mansfield shared the Nobel Prize in Physiology or Medicine in 2003 for their major contributions to the development of MRI techniques.

Nowadays, MRI is commonly used for cancer imaging, but the different NMR properties between normal tissues and tumors had been discovered even before MRI techniques were developed. In 1971, two years before Lauterbur developed the MRI technique, Damadian reported that tumors and normal tissues have different NMR properties, which could be used to diagnose cancer (8). Damadian also developed whole body NMR scanning and described the T_1 and T_2 relaxation differences in tissues which make MRI contrast feasible. In the thirty years since then, MRI has continued to grow at an incredible speed and more and more research and clinical applications of MRI have been discovered, such as when Ogawa *et al*. developed functional MRI for detecting brain neuronal activation based on the blood oxygenation level dependent or BOLD effect in 1990 (9), or when Moseley *et al*. reported that diffusion-weighted MRI (DWI) is highly sensitive to the changes occurring in the lesion of an ischemic stroke (10).

1.2 A Brief History of Diffusion and DWI

In 1828, Brown observed that pollen grains suspended in water under a microscope exhibited an erratic motion, which was subsequently named after him as Brownian motion (11). The Brownian motion remained unexplained until the kinetic theory was developed by Maxwell and Boltzmann. In one of his several world-famous papers published in 1905, Einstein combined kinetic theory and classical hydrodynamics to derive an equation that showed that the displacement of Brownian particles varies as the square root of time, which was confirmed experimentally by Perrin three years later, providing convincing evidence for the physical existence of atom-sized molecules, for which Perrin was awarded the Nobel Prize in physics in 1926.

The merging of diffusion into NMR originated in Hahn's classical spin echo paper, in which he noticed that the amplitude of the observed spin echo signal would be reduced by the random thermal motion of spins in the presence of a magnetic field inhomogeneity (4). Carr and Purcell

shortly after investigated diffusion effects on the free precession of protons and derived a set of equations to describe these diffusion effects (12). Torrey subsequently extended the Bloch equations by adding diffusion terms, and these were subsequently named the Bloch-Torrey equations (13). Nine years later, Stejskal and Tanner developed the methodology of the pulsed gradient spin echo (PGSE) experiment which made it possible to directly and quantitatively measure molecular diffusion coefficients (14). All of above works opened the window for measurements of water self-diffusion inside biological tissues. Cory used a diffusion propagator formalism and demonstrated that the size of a diffusion compartment can be obtained from diffusion NMR experiments (15). Callaghan discovered diffraction-like diffusion effects in NMR studies of materials (16). Basser *et al.* first introduced a diffusion tensor model to describe anisotropic diffusion in biological tissues (17,18). Mori *et al.* probed neuronal pathways in the rat brain by DTI (19) and introduce the concept of fiber tracking, which has proven very powerful in basic and clinical research.

Diffusion-weighted MRI (DWI) has developed since the 1980's. Taylor and Bushell first demonstrated diffusion imaging with a hen's egg in 1985 (20). LeBihan obtained early images on a whole-body system (21,22). Moseley *et al*. reported that diffusion-weighted MRI (DWI) is highly sensitive to the changes occurring in the lesion of an ischemic stroke (10) and this discovery was of significant clinical importance, and since then, DWI has attracted a lot of attention and becomes an important diagnostic tool in radiology. In 1996, Zhao *et al.* reported that the apparent diffusion coefficient (ADC) of a tumor could be used as an indicator of tumor response to treatment (23). Chenevert *et al.* used ADC measurements to monitor the early response of brain tumors (24). Nowadays, ADC has been suggested as a biomarker in cancer imaging.

1.3 Basic Principles of MRI Physics

MRI is based on the interaction of nuclear spins with an external magnetic field, $\mathbf{B}_0$. The magnetic moment of a spin processes about the field direction with an angular frequency

determined by the Larmor equation

$$\omega_0 = \gamma B_0 , \qquad [1.1]$$

where ω_0 is called the Larmor frequency and γ is the gyromagnetic ratio. (the hydrogen proton has a γ value of 2.675×10^8 rad/s/T). A static magnetic field $\mathbf{B}_0$ results a net longitudinal equilibrium magnetization $\mathbf{M}_0$, which is aligned along the $\mathbf{B}_0$ direction. If another perpendicular radiofrequency (RF) magnetic field ($\mathbf{B}_1$) (tuned to the Larmor frequency) is applied in a short time (an RF 'pulse'), spin magnetic moments will be 'tipped' away from the alignment along the $\mathbf{B}_0$ direction and towards the transverse plane, in which the magnetization will have *x* and *y* components $\mathbf{M}_x$ and $\mathbf{M}_y$, as well as $\mathbf{M}_z$ along the $\mathbf{B}_0$ direction.

The time for magnetization to recover from the excited state (with components in transverse plane) to original longitudinal equilibrium state (along $\mathbf{B}_0$ direction) is described by T_1, which is called longitudinal relaxation time or spin-lattice relaxation time. The spin-spin interaction causes the transverse magnetization decay and can be described by T_2, which is called transverse relaxation time or spin-spin relaxation time. The time evolution of magnetization in the presence of a magnetic field and with relaxation terms can be expressed by the Bloch equation (25)

$$\frac{d\mathbf{M}}{dt} = \gamma \mathbf{M} \times \mathbf{B}_{eff} + \frac{1}{T_1}(M_0 - M_z)\hat{z} - \frac{1}{T_2}\mathbf{M}_\perp \qquad [1.2]$$

The time-varying transverse magnetization induces electromotive force (*emf*) in a receive RF coil, in which the MR signals can be detected. However, the obtained signals are from the whole sample. In order to acquire MR images, it is necessary to implement Lauterbur's technique, which applies spatially dependent field (linearly dependent with a constant gradient) to encode signals. For example, if the applied field gradient is along *x* direction, the Larmor frequency becomes spatially dependent as $f(x)=\gamma(Gx+B_0)$. The detected MR signal can be expressed as

$$s(t) = \int dx \rho(x) \exp(i\phi) , \qquad [1.3]$$

where ϕ denotes the phase and $\rho(x)$ is the signal density as a function of position *x* .

$$\phi(x,t) = -\gamma x \int_0^t dt' G(t') \qquad [1.4]$$

Hence, the signal can be rewritten as

$$s(k) = \int dx \rho(x) \exp(-i2\pi kx) \qquad [1.5]$$

where

$$k = \gamma \int_0^t dt' G(t') \qquad [1.6]$$

Eq.[1.5] shows that signal is the Fourier transform of the spin density of the sample. By manipulating the gradient fields, a grid of points in *k* space can be covered and a series of corresponding signal points can be obtained. An inverse Fourier transform of those signals yields an image of sample spin density and this is the basic principle of MRI.

1.4 Basic Principles of Diffusion and DWI Physics

1.4.1 Diffusion

Einstein described an equation which relates the microscopic random motion with a macroscopically measurable phenomenon known as diffusion in 1905, which is called the Einstein relationship (11). If we consider a spin at position $\mathbf{r}'$ at time 0 and it migrates to position **r** at time τ, then the diffusion coefficient is given by

$$D = \frac{1}{6\tau} < \mathbf{r}(t=0)\mathbf{r}'(t=\tau) > \qquad [1.7]$$

where <…> denotes the average over the spin population. For a given diffusion time Δ_d, we can define a characteristic length scale

$$l = \sqrt{6D\Delta_d} \qquad [1.8]$$

l is also called the diffusion length. Notice that if we can obtain a short diffusion time Δ_d, a corresponding diffusion length can be as short as comparable to or even shorter than the characteristic length of the tissues, such as the cell sizes, which implies diffusion has the potential to probe the microscopic structures of the tissues.

1.4.2 Bloch-Torrey Equation

During the early days after the NMR phenomenon was discovered, Hahn reasoned that the random thermal motion of the spins would contribute to the attenuation of the observed spin echo signal (4). Torrey developed a continuum description based on the magnetization diffusion equation and Bloch equation, which was subsequently named as the Bloch-Torrey equation. For the transverse magnetization of interest, the Bloch-Torrey equation can written as

$$\frac{\partial \mathbf{M}_\perp}{\partial t} = -i\gamma \mathbf{g}(\mathbf{r},t)\cdot\mathbf{r}\cdot\mathbf{M}_\perp - \frac{\mathbf{M}_\perp}{T_2} + \nabla(\mathbf{D}\mathbf{M}_\perp) - \nabla\mathbf{v}\cdot\mathbf{M}_\perp, \qquad [1.9]$$

where $\mathbf{M}_\perp$ is the transverse magnetization, **D** is diffusion coefficient, $\mathbf{g}(\mathbf{r},t) = \nabla\mathbf{B}(\mathbf{r},t)$ is the applied magnetic gradient, **v** is the velocity of the fluid flow.

1.4.3 Pulsed Gradient Spin Echo (PGSE)

Stejskal and Tanner developed the pulsed gradient spin echo (PGSE) experiment (see Fig. 1-1) which made it possible to directly measure the diffusion coefficient of non-flowing fluids (14).

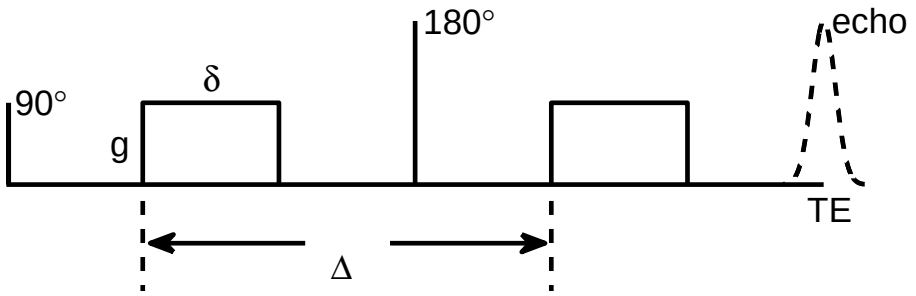

Fig. 1-1 Schematic diagram of the PGSE pulse sequence. g is the diffusion gradient amplitude, δ is the duration of one diffusion gradient and Δ is the spacing of two diffusion gradients.

The signal at the echo time is proportional to the integrated transverse magnetization, namely,

$$E(g,\vec{D}) \propto \int \bar{\mathbf{M}}_\perp(\bar{\mathbf{r}}, t = TE)d\bar{\mathbf{r}}.. \qquad [1.10]$$

If the duration of the gradient is very short and spins can be considered not diffusing during the

gradient, which is the so-called short gradient pulse approximation (SGP), Stejskal obtained an expression for free diffusion, namely,

$$\frac{E(g)}{E(g=0)} = \exp(-b \cdot D) \qquad [1.11]$$

and

$$b = (\gamma g \delta)^2 (\Delta - \delta / 3) . \qquad [1.12]$$

1.4.4 Restricted Diffusion and ADC

In biological tissues, there are many diffusion barriers such as cell membranes, and diffusion is always restricted and/or hindered. The equation [1.11] can then usefully be rewritten as

$$\frac{E(g)}{E(g=0)} = \exp(-b \cdot ADC) , \qquad [1.13]$$

where ADC is the apparent diffusion coefficient and is a function of diffusion time Δ. For free diffusion, ADC is equal to the intrinsic diffusion coefficient. ADC actually describes an averaged diffusion behavior of a restricted diffusion system. Since ADC contains some structural information, it can be used to probe microstructural features that may not be obtained by some other approaches *in vivo*.

1.4.5 Q-Space

In 1965, Stejskal suggested a conditional probability function to describe restricted diffusion analytically (26). The PGSE with the short gradient approximation then gives rise to the spin echo decay as

$$E(\mathbf{g},\Delta) = \iint \rho(\mathbf{r_0}) P(\mathbf{r_0} \mid \mathbf{r},\Delta) \exp[-i\gamma\delta \mathbf{g} \cdot (\mathbf{r_0} - \mathbf{r})] d\mathbf{r_0} d\mathbf{r} \qquad [1.14]$$

where $\rho(\mathbf{r}_0)$ is the spin density at the position $\mathbf{r}_0$, and $P(\mathbf{r}_0|\mathbf{r},\Delta)$ is the conditional probability, which is defined as the probability that a spin initially at position $\mathbf{r}_0$ (at the time of the first gradient pulse) will migrate to position $\mathbf{r}$ at $t = \Delta$ (at the second gradient pulse). With the

substitution $\mathbf{r} = \mathbf{r}_0 + \mathbf{R}$ and $\mathbf{q} = \gamma \mathbf{g} \delta$, Eq.[1.14] can be rewritten as

$$E(\Delta, \mathbf{q}) = \int \bar{P}(\mathbf{R}, \Delta) \exp(-i 2\pi \mathbf{q}\mathbf{R}) d\mathbf{R} , \qquad [1.15]$$

where $\mathbf{R}$ is the dynamic displacement and $\bar{P}(\mathbf{R}, \Delta)$ is the averaged propagator (27)

$$\bar{P}(\mathbf{R}, \Delta) = \int \rho(\mathbf{r_0}) P(\mathbf{r_0} + \mathbf{R}, \Delta) d\mathbf{r}_0 . \qquad [1.16]$$

Eq.[1.15] shows a simple Fourier relationship between the diffusion-weighted signal attenuation and the averaged propagator, which contains the microstructural information. Hence, it is possible to image the averaged propagator by signal acquisition in q-space. Cory used this diffusion propagator formalism and demonstrated that the size of a diffusion compartment can be obtained from diffusion NMR experiments (15).

In order to fit experimental data, it is plausible to derive analytical expressions to describe MR signals and, hence, the structure conditional probability function becomes the key. Usually it is very difficult to get analytical expressions of conditional probability for complex biological structures, but researchers have already derived some analytical expressions for some simple geometries. Brownstein *et al.* (28) and Balinov *et al.* (29) showed the conditional probability functions and signal attenuation dependence of some diffusion system with simple geometries, such as diffusion between two infinitely large impermeable planes or inside an infinitely-long impermeable cylinder and an impermeable sphere. Soderman *et al.* obtained solutions to diffusion inside an finitely-long impermeable cylinder (30) and Callaghan (31) extended solutions to simple geometries with particle absorption by the walls. The analytical solutions for signal attenuation enabled Callaghan to discover the diffraction-like diffusion signal attenuation in q-space (16). For example, Fig. 1-2 shows the signal attenuation caused by diffusion inside an impermeable cylinder with a radius of R and length of L, which behaves a diffraction pattern in q-space. The node positions of the diffraction pattern are dependent only on qR and such diffusion behavior provides a means to probe diffusion compartment size.

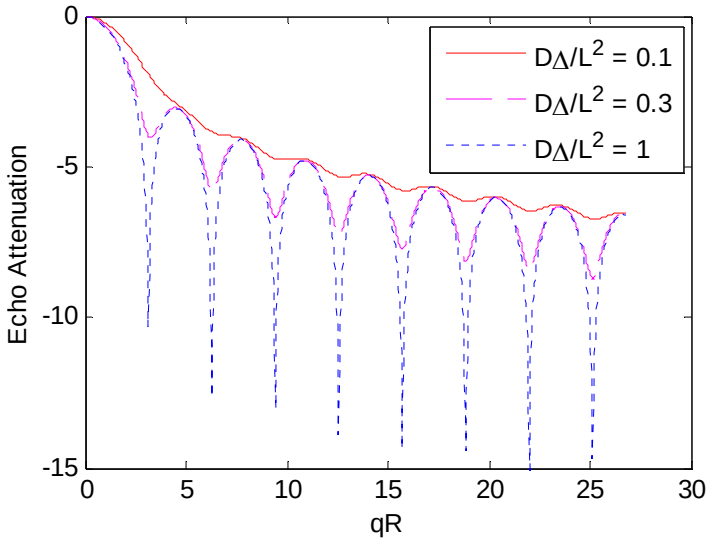

Fig. 1-2 The signal attenuation of water diffusion inside an infinitely-long impermeable cylinder behaves a diffractive-like pattern in q-space.

CHAPTER II

TEMPORAL DIFFUSION SPECTROSCOPY

The pulsed gradient spin echo (PGSE) method has been widely used in conventional diffusion studies such as measuring apparent diffusion coefficients (ADC) and diffusion tensor imaging (DTI). The signal attenuations obtained by PGSE are usually considered to be measured over a specific time interval, which is called the diffusion time Δ_d. $\Delta_d = \Delta$ if the short gradient approximation is satisfied, which means each gradient is short enough compared to Δ so that diffusion is negligible during the time the diffusion gradient is on. However, the applicable gradients have finite durations (sometimes relatively long, especially on human scanners) due to hardware limitations and, hence, the short gradient approximation is violated. Moreover, the practical diffusion gradient pulses cannot be ideally "rectangular" (i.e. with infinitely fast rise and fall times) and usually have trapezoid shapes. Therefore, the real diffusion time of the PGSE method is usually difficult to determine accurately.

An entirely different viewpoint of diffusion measurements using diffusion gradients with general shapes has been proposed by Stepisnik (32). In this approach, the diffusion-weighted signal attenuation is related to the particle velocity auto-correlation function, rather than via the propagator for displacement, which is dependent on diffusion time. Furthermore, with the frequency domain analysis, it can be shown that the diffusion spectrum is the Fourier transform of the velocity auto-correlation function and it can be "probed" by the effective gradient modulation spectrum (33). This method is named temporal diffusion spectroscopy (34) and the section 2.1 of this chapter introduces the basic principles.

According to Eq.[1.8], the diffusion time determines the diffusion length, which actually reflects the length scale that can be probed by the diffusion measurements. The practical diffusion time with PGSE is usually ten's of milliseconds corresponding to diffusion lengths on the order of 20 micrometers which reflects the influence of the restricting boundaries in the dimension much larger than typical cell sizes. However, sometimes it is important to study the intrinsic diffusion

coefficients or the intracellular diffusion that reflects the intracellular microstructures. Such studies require the diffusion lengths be shorter than the cell sizes, typically less than several microns, and the corresponding very short diffusion times usually cannot be obtained by the PGSE in practice. One approach to obtain very short diffusion times in the ADC measurements is the oscillating gradient spin echo (OGSE) method (34,35), which employs two identical successions of diffusion-weighting gradient periods, such as sine- or cosine-modulated gradients, to replace the two rectangular (trapezoidal in practice) gradients in the PGSE method. Based on the theory of temporal diffusion spectroscopy, the analytical expression of the diffusion-weighted signal attenuation with OGSE has been derived for some simple geometries, such as planes, cylinders and spheres. Such developments provide a framework to interpret the experimental data with OGSE and a means to probe tissue microstructural information. The section 2.2 of this chapter covers the principles of OGSE.

2.1 Principles of Temporal Diffusion Spectroscopy

Torrey derived the expression for diffusion-weighted signal attenuation with an arbitrary shaped gradient as (13)

$$\ln(\frac{E(t)}{E_0}) = \beta(t) = \gamma^2 D \int_0^t \left| \int_0^u G(t')dt' \right|^2 du \,. \qquad [2.1]$$

However, Eq.[2.1] is only valid for the Fick's diffusion when the duration of measurement is long compared to the correlation time of water molecules migration (36). A general echo attenuation expression which relates the velocity auto-correlation functions was introduced by Stepisnik (32).

2.1.1 Diffusion-Weighted Signal and Velocity Auto-Correlation Function

The MR signal is the sum of the spin contributions

$$E(t) = \left\langle \sum_i E_{0j} \exp(i\phi_j(\mathbf{r})) \right\rangle, \qquad [2.2]$$

where $\langle\cdot\rangle$ means the average which includes molecular motion and $\phi_j(t)$ is the spin phase, which is dependent on the effective diffusion gradient $\mathbf{G}_{eff}(t)$ and the location $\mathbf{r}_j$ of the j^{th} spin by

$$\phi_j(t) = \gamma \int_0^t \mathbf{g}_{eff}(t')[\mathbf{r}_j(t') - \mathbf{r}_0]dt' \qquad [2.3]$$

If we define the time integral of diffusion gradient as

$$\mathbf{F}(t) = \gamma \int_0^t \mathbf{g}(t')dt', \qquad [2.4]$$

and the signal attenuation can be rewritten as

$$E(2\tau) = \sum_j E_{0j} \left\langle \exp[-i \int_0^{2\tau} \mathbf{F}(t)\mathbf{v}_j(t)dt] \right\rangle, \qquad [2.5]$$

where $\mathbf{v}_j$ is the velocity of the j^{th} spin and τ is half of the echo time.

Using cumulant expansion method, Eq.[2.5] gives

$$E(2\tau) = \sum_j E_{0j} e^{i\alpha_j(2\tau) - \beta_j(2\tau) \cdots}, \qquad [2.6]$$

where

$$\alpha_j(2\tau) = -\int_0^{2\tau} \mathbf{F}(t)\left\langle \mathbf{v}_j(t) \right\rangle dt \qquad [2.7]$$

and

$$\beta_j(2\tau) = \frac{1}{2}\int_0^{2\tau}\int_0^{2\tau} \mathbf{F}(t_1)\left\langle \mathbf{v}(t_1)\mathbf{v}(t_2) \right\rangle \mathbf{F}(t_2)dt_1dt_2 . \qquad [2.8]$$

If we assume the averaged velocity of the j^{th} spin $\left\langle \mathbf{v}_j(t) \right\rangle$ is zero (Note that the averaged velocity of the whole stationary fluid is zero but the averaged velocity of individual spins is not necessarily zero. The influence of this approximation will be discussed in section 2.2.3) and, hence, Eq.[2.7] becomes zero and the diffusion-weighted signal attenuation can be expressed as

$$E(2\tau) = \exp\left\{ -\frac{1}{2}\int_0^{2\tau}\int_0^{2\tau} \mathbf{F}(t_1)\left\langle \mathbf{v}(t_1)\mathbf{v}(t_2) \right\rangle \mathbf{F}(t_2)dt_1dt_2 \right\} \qquad [2.9]$$

Eq.[2.9] shows that the diffusion-weighted signal attenuation signal relies on the velocity

auto-correlation function so that we can not only measure the diffusion coefficient but also the intermolecular interaction.

2.1.2 Frequency Domain Analysis

The spectral density of the ensemble-averaged velocity auto-correlation function is simply the diffusion spectrum

$$\mathbf{D}(\omega) = \frac{1}{2}\int_0^\infty \left\langle \mathbf{v}(t)\mathbf{v}(0)\right\rangle \exp(-i\omega t)dt\,. \qquad [2.10]$$

Hence, Eq.[2.9] becomes

$$\beta(t) = \frac{1}{\pi}\int_0^\infty \mathbf{F}(\omega)\mathbf{D}(\omega)\mathbf{F}(-\omega)d\omega\,, \qquad [2.11]$$

which simplifies, in the case of isotropic diffusion, to (33)

$$\beta(t) = \frac{1}{\pi}\int_0^\infty \mathbf{D}(\omega)\left|\mathbf{F}(\omega)\right|^2 d\omega \qquad [2.12]$$

where the spectrum of time integral of gradient modulation is given by

$$\mathbf{F}(\omega) = \int_0^t \mathbf{F}(t')\exp(-i\omega t')dt' \qquad [2.13]$$

Eq.[2.11] and [2.12] show that the diffusion-weighted signal attenuation is dependent on the diffusion spectrum and gradient modulation spectrum. By choosing appropriate diffusion gradient waveforms in the pulse sequence, the diffusion spectrum can be selectively probed at well-defined frequency ranges. Since a higher frequency corresponds to a smaller effective diffusion time, temporal diffusion spectroscopy provides a powerful and flexible analysis method to study diffusion-weighted MR.

Fig. 2-1 shows three typical diffusion gradient waveforms and their corresponding gradient modulation spectra. It is clear that most frequency components of PGSE are close to zero-frequency (DC component (33)), which corresponds to a long effective diffusion time. Sine-modulated OGSE (OGSE-sin) shows a higher spectral density at higher frequency $\pm\omega_0$,

which is the frequency of applied sine-modulated gradient waveform and, hence, OGSE-sin can probe a shorter diffusion time. The cosine-modulated OGSE (OGSE-cos) has spectral density peaks at $\pm\omega_0$ (AC component) and without DC component. Therefore, OGSE-cos has the ability to probe much shorter effective diffusion time compared with PGSE and OGSE-sin.

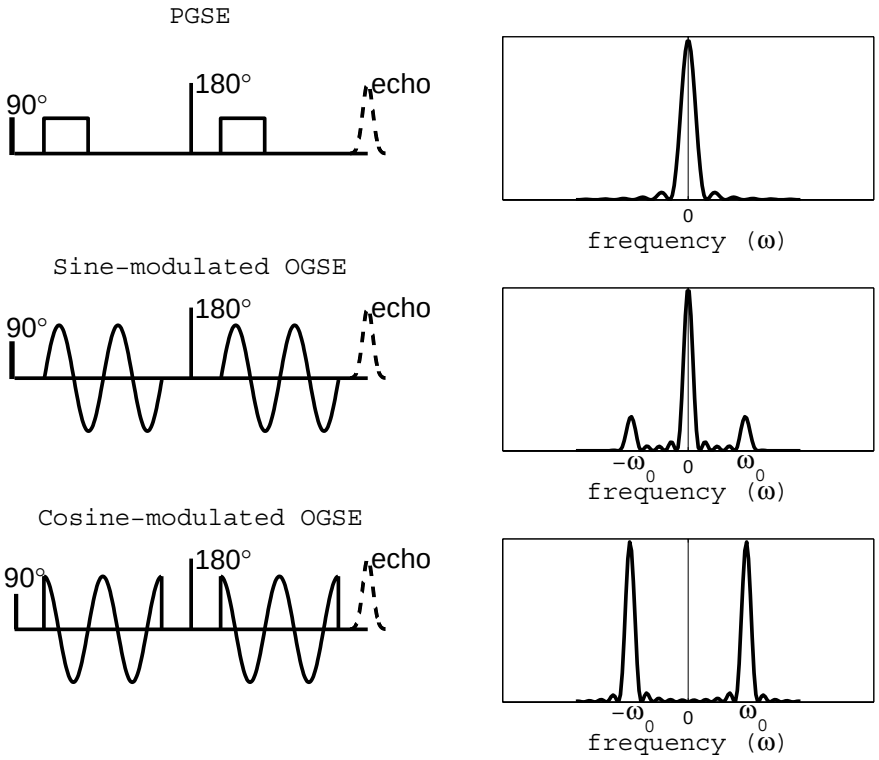

Fig. 2-1 Three typical diffusion gradient waveforms and their corresponding gradient modulation spectra.

2.1.3 Temporal Diffusion Spectroscopy with Restricted Diffusion

All diffusion temporal spectroscopy theory and equations described above are based on free diffusion. However, the importance of DWI is its ability to measure the restricted/hindered diffusion caused by diffusion barriers in biological tissues and such diffusion measurements can provide tissue microstructural information. Therefore, it is important to study temporal diffusion spectroscopy with restricted diffusion.

Eq.[2.9] can be rewritten as

$$\beta(2\tau) = \frac{1}{2}\int_0^{2\tau} dt_1 \int_0^{2\tau} dt_2 \mathbf{g}(t_1)\left\langle \mathbf{r}(t_1)\mathbf{r}(t_2)\right\rangle \mathbf{g}(t_2) \qquad [2.14]$$

If the conditional probability is known, Eq.[2.14] becomes

$$\beta(2\tau) = \frac{1}{2}\int_0^{2\tau} dt_1 \int_0^{2\tau} dt_2 \int_V d\mathbf{r} \int_V d\mathbf{r_0} \rho(\mathbf{r_0}, t_1) P(\mathbf{r_0}, t_1 \mid \mathbf{r}, t_2) \mathbf{r} g(t_1) \mathbf{r}_0 g(t_2) \qquad [2.15]$$

The conditional probability $P(\mathbf{r}_0|\mathbf{r},\Delta)$ can be expressed in a general solution form via the standard eigenmode expansion

$$P(\mathbf{r_0}, t_1 \mid \mathbf{r}, t_2) = \sum_k u_k(\mathbf{r_0}) u_k(\mathbf{r}) e^{-a_k |t_2 - t_1|}, \qquad [2.16]$$

where $u_k(\mathbf{r})$ are orthogonal solutions to the Helmholtz equation parameterized by the eignvalue a_k (31). If the gradient points in the direction defined by the unit vector $\mathbf{n}$, then $\mathbf{G}_{eff}(t) = g(t)\ \mathbf{n}$. With the substitution of Eq.[2.16] into Eq.[2.15], the signal attenuation becomes

$$\beta(2\tau) = \frac{1}{2}\sum_k B_k \int_0^{2\tau} dt_1 \int_0^{2\tau} dt_2 g(t_1) g(t_2) e^{-a_k |t_2 - t_1|}, \qquad [2.17]$$

where

$$B_k = \int_V d\mathbf{r} \int_V d\mathbf{r_0} \mathbf{n}\mathbf{r_0}\mathbf{n}\mathbf{r} u_k(\mathbf{r}) u_k(\mathbf{r}_0). \qquad [2.18]$$

B_k and a_k are structure dependent coefficients. If the conditional probability is known, the coefficients B_k and a_k can be determined. Stepisnik obtained expressions for three simple geometries. For diffusion between two impermeable infinitely-large planes separated by a distance d,

$$B_k = \frac{8d^2}{(2k-1)^4 \pi^4} \quad \text{and} \quad a_k = \frac{\pi^2 (2k-1)^2}{d^2}. \qquad [2.19]$$

For transverse diffusion inside an impermeable cylindrical geometry with a radius R,

$$B_k = \frac{2(R/\mu_k)^2}{\mu_k{}^2 - 1} \quad \text{and} \quad a_k = \left(\frac{\mu_k}{R}\right)^2, \qquad [2.20]$$

where μ_k is the k^{th} root of $J_1'(\mu) = 0$ (i.e. μ_k = 1.84, 5.33, 8.53, …)and J is the first kind Bessel

function.

For diffusion inside an impermeable spherical geometry with a radius R, the expressions for B_k and a_k are the same as a cylindrical geometry except μ_k becomes the k^{th} root of equation $\mu J'_{3/2}(\mu) - \frac{1}{2} J_{3/2}(\mu) = 0$ (i.e. μ_k = 2.08, 5.94, 9.21, …) (36).

2.2 Oscillating Gradient Spin Echo (OGSE)

2.2.1 OGSE and b Values

The signal attenuations obtained by PGSE are usually relatively long (especially on human scanners) due to hardware limitations and, hence, it is difficult to obtain short diffusion time behavior. One approach to obtain very short diffusion time is the oscillating gradient spin echo (OGSE) method (34,35), which employs two identical successions of diffusion-weighting gradient periods, such as the sine- or cosine-modulated gradients, to replace the two rectangular gradients in the PGSE method. Fig. 2-2 shows a cosine-modulated OGSE pulse. G is the amplitude of diffusion gradient, σ is the duration of each diffusion gradient pulse and corresponding b value is given by

$$b = \frac{\gamma^2 G^2 \sigma}{4\pi^2 f^2}, \qquad [2.21]$$

where f is the frequency of applied diffusion gradient.

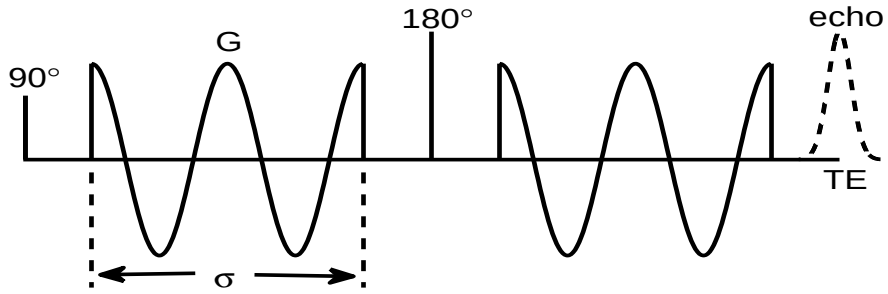

Fig. 2-2 A cosine-modulated OGSE (OGSE-cos) pulse.

In practice, in order to remove the sharp pulse edges at the start and the end of a cosine-modulated gradient, an apodised cosine-modulated gradient waveform is used, which replaces the first and the last one quarter of the cosine- by a half sine-pulse at twice the base frequency (34,37). The corresponding b values can be expressed as

$$b = \frac{\gamma^2 G^2 \sigma}{4\pi^2 f^2}(1 - \frac{1}{8N}), \qquad [2.22]$$

where N is the number of cycles in each gradient series.

As discussed in section 2.1.2 , OGSE-cos has no zero-frequency component and probes a well defined diffusion regime. Therefore, OGSE-cos has been more popularly used to obtain a short diffusion time.

2.2.2 OGSE with Restricted Diffusion

When we study tissues short time diffusion behavior, OGSE-cos is suggested to be used, which has a modulated gradient waveform as

$$g(t) = G\cos(\omega t). \qquad [2.23]$$

If we consider restricted diffusion, conditional probability should be used. Recall Eq.[2.17]

$$\beta(2\tau) = \frac{1}{2}\sum_k B_k \int_0^{2\tau} dt_1 \int_0^{2\tau} dt_2 g(t_1) g(t_2) e^{-a_k |t_2 - t_1|}$$

With substitution of Eq.[2.23] into Eq.[2.17], one can obtain

$$\beta(2\tau) = \frac{\gamma^2}{2}\sum_k B_k \int_0^{2\tau} dt_1 \int_0^{2\tau} dt_2 \cos(\omega t_1)\cos(\omega t_2) e^{-a_k |t_2 - t_1|}, \qquad [2.24]$$

which can be rewritten as

$$\begin{aligned}\beta(2\tau) = \gamma^2 \sum_k B_k \Bigg\{ & \int_0^{\sigma} dt_1 \int_0^{t_1} dt_2 \cos(\omega t_1)\cos(\omega t_2) e^{-a_k (t_1 - t_2)} + \cdots \\ & + \int_0^{\sigma} dt_1 \int_{t_1}^{\sigma} dt_2 \cos(\omega t_1)\cos(\omega t_2) e^{a_k (t_1 - t_2)} - \int_0^{\sigma} dt_1 \int_{\tau}^{\tau+\sigma} dt_2 \cos(\omega t_1)\cos(\omega t_2) e^{a_k (t_1 - t_2)} \Bigg\}\end{aligned} \qquad [2.25]$$

After some tedious derivations with the partial integration method, Eq.[2.25] becomes

$$\beta(2\tau)=\gamma^2\sum_k B_k\left\{\frac{a_kD\sigma}{2(a_k^2D^2+\omega^2)}+\frac{a_k^2D^2}{(a_k^2D^2+\omega^2)^2}(\exp(-a_kD\sigma)-1)+\cdots\right.$$
$$+\frac{a_kD\sigma}{2(a_k^2D^2+\omega^2)}-\frac{a_k^2D^2}{(a_k^2D^2+\omega^2)^2}(1-\exp(-a_kD\sigma))+\cdots \quad [2.26]$$
$$\left.+\frac{a_k^2D^2}{(a_k^2D^2+\omega^2)^2}\exp(-a_kD\tau)(2-2\cosh(a_kD\sigma))\right\}$$

After some rearrangement of Eq.[2.26], one finally can obtain

$$\beta(2\tau)=2(\gamma g)^2\sum_k\frac{B_ka_k^2D^2}{(a_k^2D^2+\omega^2)^2}\left\{\frac{(a_k^2D^2+\omega^2)\sigma}{2a_kD}-1+\exp(-a_kD\sigma)+\exp(-a_kD\tau)(1-\cosh(a_kD\sigma))\right\} \quad [2.27]$$

Recall that ω is the gradient frequency, σ the gradient duration and τ half of echo time.

Eq.[2.27] is the analytical expression for signal attenuation of OGSE-cos with restricted diffusion. If $\omega\to 0$, The OGSE pulse degenerates into conventional PGSE pulse and Eq.[2.27] becomes

$$\beta(2\tau)=2\left(\frac{\gamma g}{D}\right)^2\sum_k\frac{B_k}{a_k^2}\left\{a_kD\delta-1+e^{-a_kD\sigma}+e^{-a_kD\tau}(1-\cosh(a_kD\delta))\right\} \quad [2.28]$$

which has been reported previously (36).

Hence, we have already obtained the analytical expressions of MR measurable signal attenuation with OGSE-cos in terms of pulse sequence temporal parameters (such as ω, σ and τ), structural dependent parameters (such as B_k and a_k) and diffusion coefficient D. Once the conditional probability is known (such as for some simple structures), the explicit expression of signal attenuation can be obtained, which makes it possible to fit experimental data and extract quantitative structural parameters of the tissue, such as axon or cell size and axon proton fraction. This will be discussed in Chapter 4 .

2.2.3 Influence of Stepisnik's Approximation

Eq.[2.9] assumes that the averaged velocity $\langle \mathbf{v}_j(t)\rangle$ of j^{th} spin always equals to zero. However, this is not true because individual averaged velocity $\langle \mathbf{v}_j(t)\rangle$ of each spin is not necessarily zero

even for a stationary fluid as considered here. Although the averaged velocity of overall spins is zero, the individual averaged velocity is non-zero, which enables the contribution of $a_j(2\tau)$ (see Eq.[2.7]) to the first exponential factor in Eq.[2.6]. Hence, Eq.[2.9] is only an approximation to the exact solution because it only uses the second exponential factor term to describe the echo attenuation. Fig. 2-3 shows the comparison of finite difference simulated data and analytical data (based on Eq.[2.27]) for water perpendicular diffusion inside an infinitely-long impermeable cylinder. It is clear than there is a discrepancy between these two curves especially at relatively high b values (b > 2 ms/μm^2).

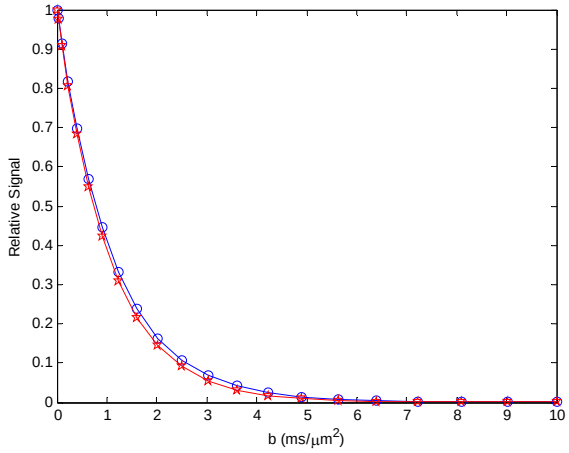

Fig. 2-3 Comparison of simulated data (circles) and analytical data (stars) for water perpendicular diffusion inside an infinitely-long impermeable cylinder.

However, the discrepancy between this approximation and the exact results is very small and can even be negligible in the presence of noise in real experiments. Besides, this approximation works well especially when b value is not large, but this is not a problem because one technical problem for OGSE is that it is not easy to obtain high b values. Therefore, Eq.[2.27] still provides us a means to study the restricted diffusion analytically and a possible way to study the restricted diffusion on the frequency-domain and get the diffusion spectra.

2.3 Conclusion

PGSE has been widely used in diffusion-weighted MRI. However, it has some limitations, due to

technical constraints, such as relatively long diffusion time. The OGSE sequence has been developed to detect short diffusion time behavior. To better understand how general shaped diffusion gradients work, temporal diffusion spectroscopy has been developed to better explain pulse sequence and better interpret experimental data. Cosine-modulated OGSE (OGSE-cos) has shown the feasibility to probe much shorter diffusion time behavior compared to PGSE and OGSE-sin and has been widely used in diffusion studies. In this chapter, the analytical expression of signal attenuation of OGSE-cos with restricted diffusion was derived. This work makes it possible to interpret OGSE experimental data and has important application in tissue modeling and data fitting, which is discussed in Chapter 4

CHAPTER III

NUMERICAL STUDY OF DIFFUSION-WEIGHTED MRI

Chapters 1 and 2 have introduced analytical solutions describing the DWI signal attenuation for some simple geometries, such as planes, cylinders and spheres. However, it is not practically possible to obtain the conditional probabilities for biological tissues so that the analytical solutions for signal attenuation usually cannot be obtained. Therefore, to better understand the factors that affect water diffusion in biological tissues with more complex morphologies, it is necessary to study the restricted diffusion numerically.

Numerical models have been previously used to study DWI, such as Monte Carlo (MC) (38) and image-based finite difference (FD) methods (39). The MC method tracks individual spins that undergo Brownian motion over a large number of time steps. On the other hand, the FD method discretizes the tissue sample into a spatial grid and updates the magnetization at each point in every time step. Sections 3.1 and 3.2 briefly introduce MC and FD methods, respectively.

Due to the failure of conventional boundary conditions (BC) for the Bloch-Torrey equation, an edge effect artifact arises with the FD method, which is caused by the introduction of artificial boundaries into the computational domain (39,40). Section 3.3 introduces an improved finite difference method, which not only implements a matrix-based FD method (MFD) that converts the conventional FD approach into a matrix-based algebra for computing efficiency, but also employs a revised periodic boundary condition to eliminate the edge effect for any diffusion-weighted pulse sequences.

Section 3.4 discusses an efficient tightly-coupled parallel computing approach, which enables large-scale FD computing for complex tissues. For comparison, different parallel computing strategies are also discussed.

Section 3.5 presents the computational error analysis and some simulation results that compare the conventional FD method and the improved FD method are introduced in section 3.6 .

3.1 Monte Carlo Method

Monte Carlo method, which is based on the first principles, uses computer-generated random numbers to simulate the random processes. When a large number of particles (usually over tens of thousands dependent on the structures) are studied this way, the results will predict the physical processes that may be experimentally determined. Szafer *et al.* numerically studied water diffusion in tissues using the Monte Carlo method in 1995 (38). The procedure of the Monte Carlo method for studying water diffusion in tissues with spin echo pulse sequence can be expressed as in the following way:

At time $t = 0$ a random uniform distribution of N particles (spins) is placed inn a system.

(1). All initial magnetizations are aligned as if just tipped by a 90° RF pulse and $\mathbf{m}_j(0^+) = \rho_j(\mathbf{r}_j)$, where j denotes the j^{th} particle, ρ_j the spin density at position $\mathbf{r}_j$. Note that only transverse magnetization is considered in the simulation for spin echo pulse sequences.

(2). Both the spin positions and magnetizations are updated in every time step.

i) The positions are updated by $\mathbf{r}_j(t+\Delta t) = \mathbf{r}_j(t) + \sqrt{6D_j \cdot \Delta t} \cdot \mathbf{r}'_j$, where $\mathbf{r}'$ is a unit vector in an arbitrary direction, D_j the intrinsic diffusion coefficient where the j^{th} particle locates and Δt is the temporal step.

ii) When the diffusion gradient is on, the magnetization is updated by $\mathbf{m}_j(t) = \mathbf{m}_j(t)\exp[-\mathrm{i}\gamma\mathbf{g}(t)\cdot\mathbf{r}_j(t)\Delta t]$, where $\mathbf{g}(t)$ is the diffusion gradient at time t.

iii) In each time step, the transverse magnetization decays in the way of $\mathbf{m}_j(t+\Delta t) = \mathbf{m}_j(t)\exp[-\Delta t / T_{2,j}]$, where T_2 is the transverse relaxation time of the compartment that the j^{th} particle is in.

iv) When a particle encounters a membrane, it has a probability to cross the membrane so that its position and magnetization must be revaluated. The membrane permeability, P_m, and the transmission probability $p_{i\to e}$ and $p_{e\to i}$ are related by the formula $P_m = \frac{1}{4}v_i p_{i\to e} = \frac{1}{4}v_e p_{e\to i}$, where v_i and v_e are intra- and extracellular particle

velocities, respectively.

(3). The echo signal is finally calculated by $E(q=\gamma g\delta, TE)=\left|\sum_{j=1}^{N}\mathbf{m}_j(TE)\right|$.

Fig. 3-1 shows that Monte Carlo simulated results have some oscillating behaviors different from the analytical results. When more particles are simulated, from 10^4 to 10^5, the simulated results are closer to the analytical ones but still quite different. This behavior can be explained in the following way. In the Monte Carlo simulation, a population of particles distributes in the whole system and the particles that encounter the membranes actually are only a quite small portion of all the particles so that the echo signal does not contain enough information about the tissue features that restrict diffusion. Hence, to solve this problem, more particles should be considered in the simulation or, equivalently, the same simulation should be run many times to obtain an accurate average result. Hence, the MC method is usually time consuming and a more efficient numerical method is desirable.

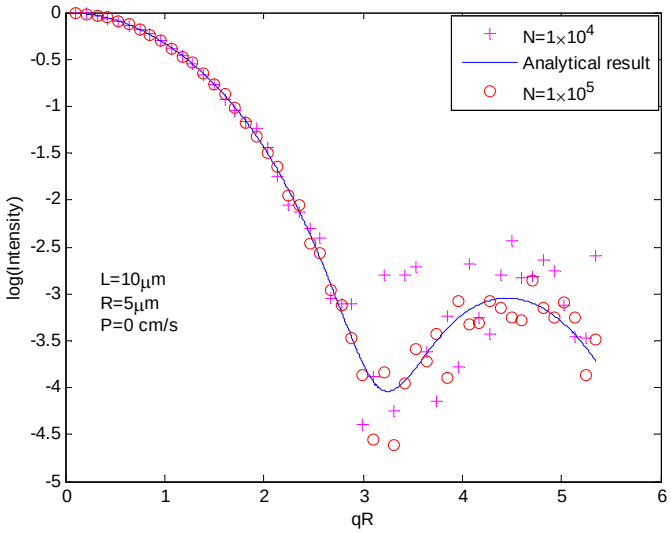

Fig. 3-1 Monte Carlo simulation results of perpendicular diffusion inside an impermeable cylinder. *N* is the number of spins used in the simulations, *L* length of cylinder, *R* radius of cylinder and *P* is permeability of cylinder walls.

3.2 Conventional Finite Difference Method

3.2.1 Finite difference Method

The FD method solves partial differential equations (PDE) on a spatial grid over a series of time steps. In DWI, the main PDE is the Bloch-Torrey equation. Hwang *et al.* developed an image-based finite difference (FD) method to study the restricted diffusion (39). In a forward time centered space (FTCS) discretization scheme (41) in a 1D 3-point finite difference stencil (see Fig. 3-2), the Bloch-Torrey equation can be rewritten as (For simplicity, only 1D formulae are considered below, but 2D and 3D cases can be easily derived in a similar way)

$$m_j^{n+1} = \exp(-\Delta t / T_{2,j}) \exp(-\mathrm{i}\gamma g^n x_j \Delta t) \cdot m_j'^{n+1} \qquad [3.1]$$

and

$$m_j'^{n+1} = (1 - 2\frac{D_x \Delta t}{\Delta x^2}) m_j^n + \frac{D_x \Delta t}{\Delta x^2} m_{j+1}^n + \frac{D_x \Delta t}{\Delta x^2} m_{j-1}^n \qquad [3.2]$$

where $m = M_x + \mathrm{i}M_y$, i is the imaginary unit, γ is the gyromagnetic ratio for hydrogen, superscript n indicates the temporal indices, subscript j the spatial index, D_x indicates the diffusion coefficients along the x direction and $T_{2,j}$ is the transverse relaxation time at point (j). Eq.[3.1] describes the transverse relaxation and the phase accumulation during the application of diffusion-sensitizing gradients and Eq.[3.2] describes the diffusion process itself. Since Eq.[3.1] is relatively easy to handle, the focus of this work is on Eq.[3.2] which deals only with the magnetization diffusion.

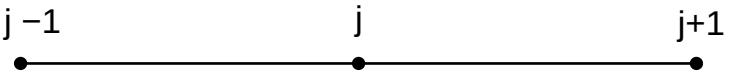

Fig. 3-2 A 1D 3-point finite difference stencil.

Note that Eq.[3.2] assumes diffusion coefficients are homogeneous. However, the diffusion coefficients are not homogeneous for biological tissues and jump probabilities must be used to describe the movement of water molecules between grid points (39). The jump probability is defined as the probability that a spin starts at one grid point and migrates to another point after a

time interval Δt. The jump probabilities in one diffusion compartment can be defined as

$$s_x = \frac{D_x \Delta t}{\Delta x^2}, \quad s_y = \frac{D_y \Delta t}{\Delta y^2} \quad \text{and} \quad s_z = \frac{D_z \Delta t}{\Delta z^2} \qquad [3.3]$$

If the two adjacent grid points, 1 and 2, are in different compartments, the jump probability between them can be expressed as

$$s_{1\to 2} = \frac{2\Delta t}{\Delta x^2} \frac{D_1 D_2 P_m c_f c_2 \Delta x}{D_1 c_1 c_f P_m \Delta x + 2 D_1 c_1 D_2 c_2 + D_2 c_2 c_f P_m \Delta x}, \qquad [3.4]$$

where P_m is the permeability of the membrane, c_f is the free concentration of water. Therefore, Eq.[3.2] may then be expressed in terms of the jump probabilities as

$$m_j'^{n+1} = (1 - s_{j\to j-1} - s_{j\to j+1}) m_j^n + s_{j-1\to j} m_{j-1}^n + s_{j+1\to j} m_{j+1}^n \qquad [3.5]$$

where $s_{j\to j-1}$ is the jump probability from point (j) to (j-1).

The FD method was implemented to simulate water perpendicular diffusion inside an infinitely-long impermeable cylinder and results shown in Fig. 3-3.

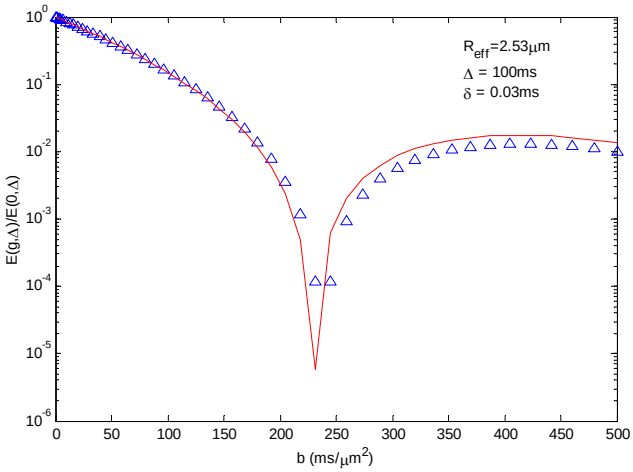

Fig. 3-3 Simulated (triangles) and analytical (line) signal attenuation versus b values for diffusion inside a infinitely-long cylinder.

3.2.2 Edge Effect

Most applications of FD methods rely on three basic boundary conditions, Dirichlet, Neumann

and periodic. The first one assumes that the function values at the boundaries are predictable; the second one assumes the fluxes across the boundaries are predictable; and the third assumes the fluxes entering and leaving are equal. However, the applied magnetic gradients in the Bloch-Torrey equation break down the applicability of all these conventional boundary conditions because the magnetic gradients make the local magnetization increments dependent on location, so that after some time of undergoing Brownian motion, neither the magnetizations at the boundaries nor the magnetization fluxes across the boundaries are predictable and the magnetizations in the computational domain obviously do not conserve. If an assumption of impermeable boundaries is used, the apparent diffusion close to those artificial boundaries is highly restricted. Therefore, the simulated signals are enhanced significantly by error. This is the so called "edge effect", noted by Hwang, *et al* (2003). To avoid the edge effect, they obtained results only from the unaffected central one third grid points for a specific diffusion time (37*ms*). However, when the diffusion time increases the influence of the boundaries propagates further into the center of the computational domain, and then the central one third region no longer produces reliable data. In this case, fewer grid points can be chosen or, equivalently, an even larger computational domain is necessary. This is either computationally expensive or a source of significant errors.

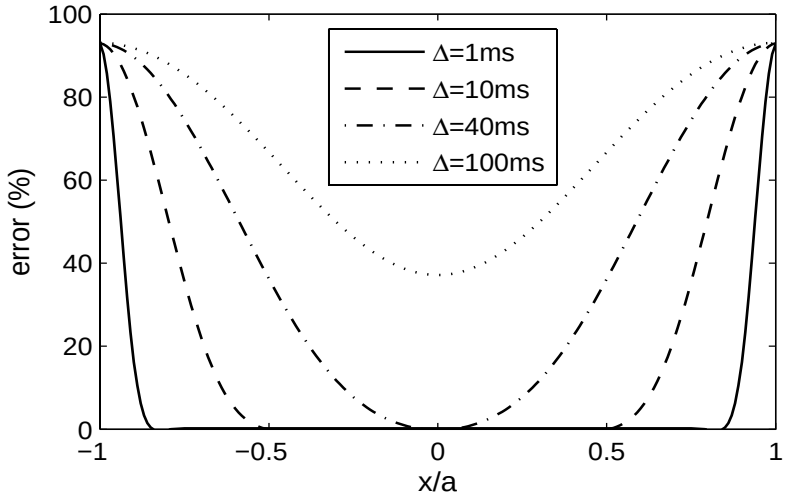

Fig. 3-4 Error distributions of simulated magnetization as a function of spatial coordinates x and diffusion times using the conventional FD method.

Fig. 3-4 shows how the edge effect increases with increasing diffusion time when using the conventional FD method. The error is expressed as the ratio $|ADC_{simulated} - ADC_{ideal}|/ADC_{ideal} \times 100\%$ and the simulated parameters are diffusion coefficient D = 1 μm^2/ms, b = 1 ms/μm^2, Δx = 0.2 μm, $\Delta t = 10^{-3}$ ms and a = 20 μm. Hence, edge effects cause more artifact with long diffusion times and they must either be reduced by additional computation over an extended domain or they become a source of significant errors. This shortcoming limits the practical usage of FD methods.

3.3 Improved Finite Difference Method

3.3.1 Matrix-Based Finite Difference Method

Eq.[3.5] focuses on the individual grid points, but it can be rewritten in a more convenient way. If we label grid points with 1, 2, 3, …, N, (N is the total number of grid points, shown in Fig. 3-5) and suppose there are impermeable barriers at boundaries (this is how conventional FD deals with the boundaries, which causes edge effects), the FD equations with explicit FTCS are given by

$$m_1'^{n+1} = m_1^n - s_{1\to 2} m_1^n + s_{2\to 1} m_2^n$$

$$m_2'^{n+1} = m_2^n - (s_{2\to 1} + s_{2\to 3}) m_2^n + s_{1\to 2} m_1^n + s_{3\to 2} m_3^n$$

$$m_3'^{n+1} = m_3^n - (s_{3\to 2} + s_{3\to 4}) m_3^n + s_{2\to 3} m_2^n + s_{4\to 3} m_4^n$$

$$\vdots$$

$$m_N'^{n+1} = m_N^n - s_{N\to N-1} m_N^n + s_{N-1\to N} m_{N-1}^n$$

Alternatively, the matrix form of Eq.[3.5] may be written as

$$\mathbf{M}'^{n+1} = \mathbf{M}^n + \mathbf{A}\mathbf{M}^n \qquad [3.6]$$

where $\mathbf{M}^n$ denotes a vector containing magnetizations and the transition matrix $\mathbf{A}$, which contains the biological tissue structural information, is given by

$$\begin{pmatrix} -s_{1\to 2} & s_{2\to 1} & 0 & \cdots & 0 \\ s_{1\to 2} & -s_{2\to 1}-s_{2\to 3} & s_{3\to 2} & \cdots & 0 \\ 0 & s_{2\to 3} & -s_{3\to 2}-s_{3\to 4} & \cdots & 0 \\ \vdots & \vdots & \vdots & \ddots & 0 \\ 0 & 0 & 0 & \cdots & -s_{N\to N-1} \end{pmatrix} \quad [3.7]$$

Note that Eq.[3.7] gives the maximum possible number of non-zero elements. If any two grid points do not exchange water molecules in a time step, the corresponding matrix element should be zero.

Finally, the discretized Bloch-Torrey equation for transverse magnetization using the MFD with explicit FTCS scheme can be written as

$$\mathbf{M}^{n+1} = \mathbf{\Phi}^n \otimes (\mathbf{I} + \mathbf{A})\mathbf{M}^n, \quad [3.8]$$

where $\mathbf{I}$ is an identity matrix with the same size of $\mathbf{A}$, $\otimes$ denotes the element-by-element vector multiplication and $\mathbf{\Phi}^n$ is a vector describing the phase accumulation and the transverse relaxation in every time step,

$$\mathbf{\Phi}^n = \left[\exp(-\mathrm{i}\gamma g^n x_1 \Delta t - \Delta t / T_{2,1}), \exp(-\mathrm{i}\gamma g^n x_2 \Delta t - \Delta t / T_{2,2}), \cdots, \exp(-\mathrm{i}\gamma g^n x_N \Delta t - \Delta t / T_{2,N}) \right] \quad [3.9]$$

Eq.[3.8] converts the conventional FD formulism into matrix algebra which not only simplifies the notation, making it easier to implement into a simulation, but also increases the computing efficiency because most of the scientific languages such as MATLAB and C/C++, have optimized packages/subroutines for computing with large matrices. Moreover, different discretization schemes can be easily implemented using MFD. For example, MFD with the implicit FTCS is expressed as

$$\mathbf{M}^{n+1} = \mathbf{\Phi}^n \otimes (\mathbf{I} - \mathbf{A})^{-1}\mathbf{M}^n, \quad [3.10]$$

and with the Crank-Nicolson scheme (41) it is

$$\mathbf{M}^{n+1} = \mathbf{\Phi}^n \otimes (\mathbf{I} - \frac{\mathbf{A}}{2})^{-1}(\mathbf{I} + \frac{\mathbf{A}}{2})\mathbf{M}^n \quad [3.11]$$

Another benefit from MFD is that the boundary conditions can be included in the matrix $\mathbf{A}$. Since most of the simulations deal with invariable structures, such as image-based FD simulations, the matrix $\mathbf{A}$ can be determined at the start of simulation and that increases the computing efficiency

significantly. Note that **A** has the dimensions of $N \times N$ which is usually extremely large and a sparse matrix should be used to avoid any possible memory allocation problems in the simulation.

3.3.2 Revised Periodic Boundary Condition (RPBC)

A possible solution to reduce the edge effect is the hybrid discretization scheme algorithm (HDSA) (42). However, HDSA still induces errors at the boundaries and, moreover, it becomes less stable when high b values (>100ms/μm^2) are used. A revised periodic boundary condition (RPBC) for the Bloch-Torrey equation has been developed to eliminate the edge effect completely.

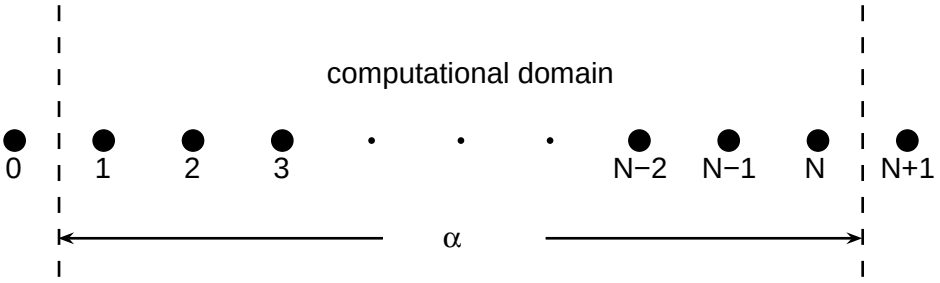

Fig. 3-5 Diagram scheme of the 1D revised periodic boundary condition. The region between two dashed lines is the computational domain. The whole structure is periodic so that point 0 and N, point 1 and N+1 have identical structures and spin densities, respectively.

3.3.2.1 Periodic Structure and Magnetization Distribution

On the assumption that the structure is periodic with the computational domain as the unit cell, a simple relationship can be derived between any two corresponding points in different unit cells with any gradient waveforms. For simplicity, only 1D case was discussed below. 2D and 3D cases can be derived in a similar way.

Suppose x_a and x_b are two points related with

$$x_a = x_b + n\alpha \,, \qquad [3.12]$$

where n is any integer and α is the length of the unit cell. The water diffusion propagator of the

whole periodic structure can be defined as $P(x|\ x',\ \Delta)$ which means the probability of a water molecule starts from position x and migrates to x' after a diffusion time Δ. The explicit form of the propagator is usually unknown except for a few simple geometries. However, the periodic structure yields

$$P(x \mid x', \Delta) = P(x + n\alpha \mid x' + n\alpha, \Delta)\,, \qquad [3.13]$$

transverse relaxation time

$$T_2(x) = T_2(x + n\alpha)\,, \qquad [3.14]$$

and the spin density

$$\rho(x) = \rho(x + n\alpha)\,. \qquad [3.15]$$

Since any general gradient waveform can be considered as a series of short gradients (43,44), the magnetizations at x_a and x_b can be calculated by

$$\begin{aligned} m(x_a,t) = \int dx_1 \int dx_2 \cdots \int dx_N \rho(x_1) \exp(-\mathrm{i}q_1 x_1) \exp(-\Delta t / T_2(x_1)) P(x_1 \mid x_2, \Delta t) \cdots \\ \times \exp(-\mathrm{i}q_2 x_2) \exp(-\Delta t / T_2(x_2)) P(x_2 \mid x_3, \Delta t) \cdots \\ \times \exp(-\mathrm{i}q_{N-1} x_{N-1}) \exp(-\Delta t / T_2(x_{N-1})) P(x_{N-1} \mid x_N, \Delta t) \cdots \\ \times \exp(-\mathrm{i}q_N x_N) \exp(-\Delta t / T_2(x_N)) P(x_N \mid x_a, \Delta t) \end{aligned} \qquad [3.16]$$

and

$$\begin{aligned} m(x_b,t) = \int dx_1 \int dx_2 \cdots \int dx_N \rho(x_1) \exp(-\mathrm{i}q_1 x_1) \exp(-\Delta t / T_2(x_1)) P(x_1 \mid x_2, \Delta t) \cdots \\ \times \exp(-\mathrm{i}q_2 x_2) \exp(-\Delta t / T_2(x_2)) P(x_2 \mid x_3, \Delta t) \cdots \\ \times \exp(-\mathrm{i}q_{N-1} x_{N-1}) \exp(-\Delta t / T_2(x_{N-1})) P(x_{N-1} \mid x_N, \Delta t) \cdots \\ \times \exp(-\mathrm{i}q_N x_N) \exp(-\Delta t / T_2(x_N)) P(x_N \mid x_b, \Delta t) \end{aligned} \qquad [3.17]$$

where $q_n = \gamma g_n \Delta t$, n=1 … N, g_n is the gradient at time t_n , Δt is the time step and $t = N\Delta t$, N is the total number of time steps. Considering the periodic structure, a substitution of $x_N = x_N' + n\alpha$ and [3.12] can be made and [3.16] becomes

$$\begin{aligned} m(x_a,t) = \exp(-\mathrm{i}n\alpha q_N) \int dx_1 \int dx_2 \cdots \int dx_N' \rho(x_1) \exp(-\mathrm{i}q_1 x_1) \exp(-\Delta t / T_2(x_1)) P(x_1 \mid x_2, \Delta t) \cdots \\ \times \exp(-\mathrm{i}q_2 x_2) \exp(-\Delta t / T_2(x_2)) P(x_2 \mid x_3, \Delta t) \cdots \\ \times \exp(-\mathrm{i}q_{N-1} x_{N-1}) \exp(-\Delta t / T_2(x_{N-1})) P(x_{N-1} \mid x_N' + n\alpha, \Delta t) \cdots \\ \times \exp(-\mathrm{i}q_N x_N') \exp(-\Delta t / T_2(x_N')) P(x_N' \mid x_b, \Delta t) \end{aligned} \qquad [3.18]$$

After a series of substitutions $x_j = x_j' + n\alpha$ (j = N-1, N-2, …, 1), Eq.[3.18] becomes

$$
\begin{aligned}
m(x_a,t) = \exp(-\mathrm{i}n\alpha\sum_{k=1}^{N} q_k)\int dx_1'\int dx_2'\cdots\int dx_N'\rho(x_1')\exp(-\mathrm{i}q_1x_1')\exp(-\Delta t/T_2(x_1'))P(x_1'\mid x_2',\Delta t)\cdots \\
\times\exp(-\mathrm{i}q_2x_2')\exp(-\Delta t/T_2(x_2'))P(x_2'\mid x_3',\Delta t)\cdots \\
\times\exp(-\mathrm{i}q_{N-1}x_{N-1}')\exp(-\Delta t/T_2(x_{N-1}'))P(x_{N-1}'\mid x_N',\Delta t)\cdots \\
\times\exp(-\mathrm{i}q_Nx_N')\exp(-\Delta t/T_2(x_N'))P(x_N'\mid x_b',\Delta t) \\
= \exp(-\mathrm{i}n\alpha\sum_{k=1}^{N} q_k)m(x_b,t)
\end{aligned}
\qquad [3.19]
$$

In general, one can obtain

$$
m(x_a,t) = \exp[-\mathrm{i}n\alpha\gamma\int_0^t g(t')dt']\cdot m(x_b,t)\,. \qquad [3.20]
$$

Recall that $x_a = x_b + n\alpha$. Eq.[3.20] shows that the magnetizations at two corresponding points in different unit cells are simply related with a phase factor which depends only on the integral of the applied diffusion gradients and the distance between these two points. Note that it is assumed that the whole structure is periodic but the structure inside each unit cell (the computational domain) is usually heterogeneous.

3.3.2.2 Revised Periodic Boundary Condition (RPBC)

Fig. 3-5 shows the schematic diagram of the RPBC. The length of the computational domain is α which is the length of a unit cell. The conventional periodic boundary condition, $m_0 = m_N$ and $m_{N+1} = m_1$, is obviously not correct for our problem. However, using the relation of two corresponding points in a periodic structure discussed above (Eq.[3.20]), we obtain

$m_0^n = \exp[\mathrm{i}\alpha\gamma\sum_{k=1}^{n} g^k\Delta t]\cdot m_N^n$ and $m_{N+1}^n = \exp[-\mathrm{i}\alpha\gamma\sum_{k=1}^{n} g^k\Delta t]\cdot m_1^n$. Hence, the updating rules for the edge points 1 and N become

$$
m_1'^{n+1} = m_1^n - (s_{1\to 2}+s_{1\to N})m_1^n + s_{2\to 1}m_2^n + s_{N\to 1}\exp(\mathrm{i}\alpha\gamma\sum_{k=0}^{n} g^k\Delta t)m_N^n \qquad [3.21]
$$

and

$$m_N'^{n+1} = m_N^n - (s_{N\to N-1} + s_{N\to 1}) m_N^n + s_{N-1\to N} m_{N-1}^n + s_{1\to N} \exp(-\mathrm{i}\alpha\gamma \sum_{k=0}^{n} g^k \Delta t) m_1^n , \quad [3.22]$$

where $s_{1\to N}$ and $s_{N\to 1}$ are defined as the jump probabilities between points 1 and N as if they were adjacent. Eqs. [3.21] and [3.22] are the RPBC for 1D Bloch-Torrey equation. Since the only assumption here is the periodic structure, this RPBC can be used for any gradient waveforms.

The transition matrix **A** with the RPBC becomes

$$\begin{pmatrix} -s_{1\to 2} - s_{1\to N} & s_{2\to 1} & 0 & \cdots & s_{N\to 1} \exp(\mathrm{i}\alpha\gamma \sum_{k=1}^{n} g^k \Delta t) \\ s_{1\to 2} & -s_{2\to 1} - s_{2\to 3} & s_{3\to 2} & \cdots & 0 \\ 0 & s_{2\to 3} & -s_{3\to 2} - s_{3\to 4} & \cdots & 0 \\ \vdots & \vdots & \vdots & \ddots & 0 \\ s_{1\to N} \exp(-\mathrm{i}\alpha\gamma \sum_{k=1}^{n} g^k \Delta t) & 0 & 0 & \cdots & -s_{N\to N-1} - s_{N\to 1} \end{pmatrix} \quad [3.23]$$

With the substitution of Eq.[3.23], the RPBC is easy to implement into Eq.[3.8] (explicit FTCS), Eq.[3.10] (implicit FTCS) and Eq.[3.11] (Crank-Nicolson) for solving the Bloch-Torrey equation. For the conventional FD method, the transition matrix **A** remains invariant for a certain tissue sample which significantly increases the computing efficiency. In contrast, for the improved FD with RPBC method, **A** depends on the applied gradients, which are usually time-dependent. Hence, extra computing time should be used to update **A** in every time step if a general diffusion-sensitizing gradient waveform is used for the RPBC method. This may decrease computing efficiency. Fortunately, only the matrix elements which describe the diffusion across the boundaries vary and they usually take only a small portion of the total matrix elements. Therefore, the extra time spent on updating **A** in the RPBC method increases only a small portion of the total computing time. Furthermore, the RPBC method significantly reduces the effective dimension of the tissue sample by removing the edge effects. Hence, the improved FD with RPBC method shows a better computing efficiency than the conventional FD method. In practice, the explicit FTCS discretization scheme is suggested for the improved FD with RPBC method to avoid the time-consuming calculations of matrix inversion in implicit FTCS or Crank-Nicolson schemes.

3.4 Parallel Computing

The intrinsic diffusion coefficients inside cells may be different from those outside the cells and it has already been shown that membrane permeability plays an important (maybe dominant) role in water diffusion in biological tissues (45). Therefore, the computational model should have a space resolution at least of the cellular level. In order to probe what intracellular structures affect diffusion, the resolution must be even greater and cells cannot be considered uniform or isotropic. Considering the small cellular dimensions of brain tissue (e.g. 2μm for gray matter) and relatively large spatial resolution of DWI (> 100μm, typically), the computing problem has very large scale; > 10^6 nodes even for one voxel of an MRI image. Hence, a high performance computing technique is necessary to extend numerical methods suitable to larger-scale samples. We have implemented a parallel processing approach to address this problem.

The most time-consuming part in solving Eq.[3.8], [3.10] or [3.11] is the matrix-vector multiplication which therefore should be parallelized. There are several frequently used parallel models, and among them, the master-slave model is one of the most popularly used (46).

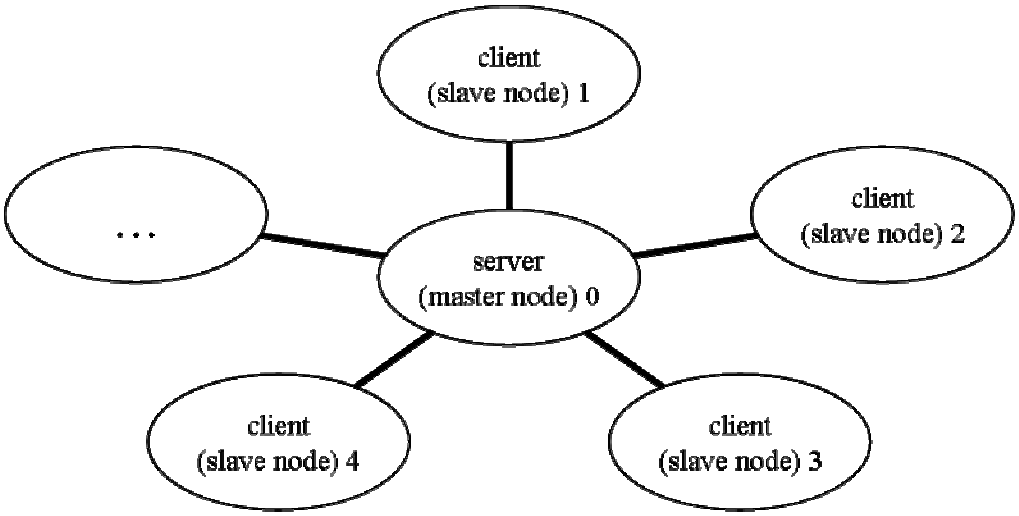

Fig. 3-6 The virtual topology of the server/client (or master/slave) parallel model

Fig. 3-6 shows the virtual topology of the server/client parallel model. The server (node 0) plays the most important role in this model. It loads jobs, decides how to assign jobs to the client nodes,

reaps results when the client nodes complete and finally output or save the results to the disk. Hence, this model is suitable for a bunch of small- or medium-scale computing jobs. For example, it is usually important to get the dispersion curve of ADC vs. diffusion gradient frequency ω. We can use this model to simulate ADCs using each client to simulate the echo attenuation only corresponding to one ω value and, then the server collects all results from clients and outputs the dispersion curve. However, this model might not be the efficient way for our problem due to the large dimension of our computing sample, we need to use some other parallel computing models.

An alternate parallelization strategy for our problem can be expressed as (47)

$$\begin{pmatrix} 1 \\ \hline 2 \\ \hline \vdots \\ \hline n_p \end{pmatrix} \times \begin{pmatrix} 1 \\ - \\ 2 \\ - \\ \vdots \\ - \\ n_p \end{pmatrix} \qquad [3.24]$$

1, 2, …, denote the indices of strips calculated by corresponding processors and n_p is the total number of processors. This method splits the large matrices and vectors into smaller strips and one processor computes one strip so that the effective dimension of the problem is decreased. However, this method requests all processors to broadcast all their results to the other processors in every time step which is usually a bottleneck for the computing. To decrease the communication among processors and increase the computing efficiency, a tightly-coupled parallel computing model was developed for our problem.

In this model, the whole sample tissue is first partitioned into a number of small sub-blocks (cubes in Fig. 3-7) according to the number of processors so that each sub-block is simulated by a single processor. Obviously, the processors are organized into a 3-D Cartesian virtual topology which is the same as the topology of sub-blocks. Every processor simulates one sub-block using the MFD described in Section 3.3.1 as if it was a single processor problem. However, the sample partition induces new artificial boundaries between the sub-blocks which usually cause larger errors. To avoid this influence, all of the processors should work synchronously and

communicate with adjacent processors to swap boundary information in every time step. The effect of the new-formed artificial boundaries can be completely eliminated. For the boundaries of the whole computational domain, RPBC should be used to eliminate the edge effect. Hence, our tightly-coupled parallel computing model does not induce any more errors in the simulation. Note that the communication burden of the tightly-coupled model is of the order of $\sum_{m,n} N_m N_n,\ (m,n = x,y,z)$, which is usually much less than the amount of [3.24] ($N_x N_y N_z$) and that is the reason why this model shows an increased efficiency.

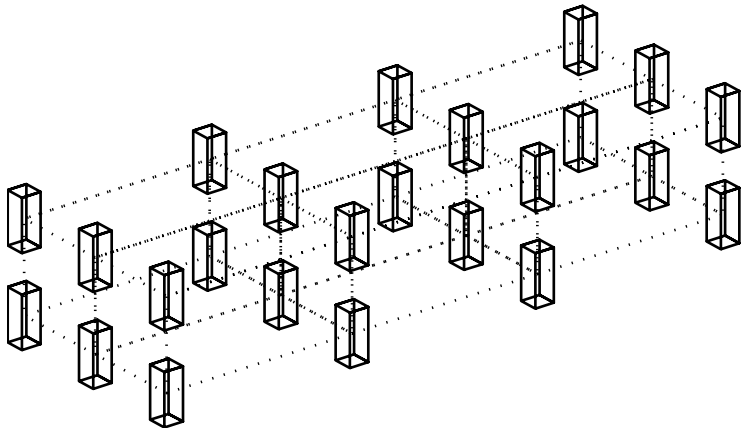

Fig. 3-7 Topology of tightly-coupled parallel computing model. Cubes represent the sub-blocks processed by different processors. The virtual topology of processors should be the same and dotted lines represent the communications between adjacent processors.

The tightly-coupled parallel computing approach significantly reduces the communication overhead in the simulation and increases the parallel computing performance. In addition, since all simulations in this dissertation were performed with a Gigabit Ethernet network, an even better parallel computing performance may be obtained by using a Myrinet network (which has lower latency and higher band-width).

3.5 Computational Error Analysis

To employ revised periodic boundary condition (RPBC), the forward time centered space (FTCS)

discretization scheme is suggested to implement in order to reduce the computing time for updating the matrix **A** (see Eq.[3.23]). When the FD method with explicit FTCS scheme is used, the Courant-Friedrichs-Lewy (CFL) condition (41) should be satisfied to ensure the stability of the simulation, i.e., jump probability should be smaller or equal to 1/2, 1/4, 1/6 for 1D, 2D and 3D, respectively. However, it has been found in simulation that the amplitudes of the applied magnetic gradients affect the results: larger amplitude gradients yield larger errors (48). Therefore, it is important to study the computational errors in order to obtain more accurate results in the simulations.

3.5.1 Consistence Error

The consistence error is defined as the difference of the simulated result and the exact solution. It's obvious that we'd better get as small consistence error as possible in the simulation. For a conventional diffusion equation, the consistence error can be expressed as (41)

$$Error_i^n = 0.5\alpha\Delta x^2(s-\frac{1}{6})\left[\frac{\partial^4\bar{\mathbf{M}}}{\partial x^4}\right]_i^n + O(\Delta t^2, \Delta x^4). \qquad [3.25]$$

Hence, s is usually chosen as 1/6 to minimize the consistence error in a conventional diffusion equation. However, in our work, the Bloch-Torrey equation (see Eq.[1.9]) is the governing equation and the consistence error should be re-analyzed. To simplify the analysis, only 1D situation is considered here. 2D and 3D analysis can be obtained in a similar way. The 1D Bloch-Torrey equation with FTCS discretization scheme can be expressed as

$$\mathbf{M}_j^{n+1} = -\mathrm{i}\gamma x_j g^n \Delta t \mathbf{M}_j^n + \frac{D}{\Delta x^2}(\mathbf{M}_{j+1}^n + \mathbf{M}_{j-1}^n - 2\mathbf{M}_j^n) + \mathbf{M}_j^n \qquad [3.26]$$

Considering the Taylor series expansions about the (j,n)-th node for each term of the 1D Bloch-Torrey equation produces, one can obtain

$$\bar{\mathbf{M}}_j^{n+1} = \bar{\mathbf{M}}_j^n + \Delta t\left[\frac{\partial\bar{\mathbf{M}}}{\partial t}\right]_j^n + \frac{\Delta t^2}{2}\left[\frac{\partial^2\bar{\mathbf{M}}}{\partial t^2}\right]_j^n + O(\Delta t^3) \qquad [3.27]$$

and

$$\vec{\mathbf{M}}_{j\pm1}^{n} = \vec{\mathbf{M}}_{j}^{n} \pm \Delta x\left[\frac{\partial \vec{\mathbf{M}}}{\partial x}\right]_{j}^{n} + \frac{\Delta x^2}{2}\left[\frac{\partial^2 \vec{\mathbf{M}}}{\partial x^2}\right]_{j}^{n} \pm \frac{\Delta x^3}{6}\left[\frac{\partial^3 \vec{\mathbf{M}}}{\partial x^3}\right]_{j}^{n} + \frac{\Delta x^4}{24}\left[\frac{\partial^4 \vec{\mathbf{M}}}{\partial x^4}\right]_{j}^{n} + O(\Delta x^5) \qquad [3.28]$$

With the substitution of Eq.[3.27] and Eq.[3.28] into Eq.[3.26] and after some rearrangements, one can get

$$\vec{\mathbf{M}}_{j}^{n} + i\gamma g^{n} x_j \vec{\mathbf{M}}_{j}^{n} - D\left[\frac{\partial^2 \vec{\mathbf{M}}}{\partial x^2}\right]_{j}^{n} + \frac{\Delta t^2}{2}\left[\frac{\partial^2 \vec{\mathbf{M}}}{\partial t^2}\right]_{j}^{n} - \frac{D\Delta x^2}{12}\left[\frac{\partial^4 \vec{\mathbf{M}}}{\partial x^4}\right]_{j}^{n} + O(\Delta t^2, \Delta x^4) = 0 \qquad [3.29]$$

With the comparison of Eq.[3.29] and Eq.[3.26], the consistency error caused by the (*j*,*n*)-th node can be defined as

$$E_{j}^{n} = \frac{\Delta t^2}{2}\left[\frac{\partial^2 \vec{\mathbf{M}}}{\partial t^2}\right]_{j}^{n} - \frac{D\Delta x^2}{12}\left[\frac{\partial^4 \vec{\mathbf{M}}}{\partial x^4}\right]_{j}^{n} + O(\Delta t^2, \Delta x^4) \qquad [3.30]$$

Notice that

$$\begin{aligned} \frac{\partial^2 \vec{\mathbf{M}}}{\partial t^2} &= \frac{\partial}{\partial t}\left(\frac{\partial \vec{\mathbf{M}}}{\partial t}\right) = \frac{\partial}{\partial t}\left(-i\gamma g x \vec{\mathbf{M}} + D\frac{\partial^2 \vec{\mathbf{M}}}{\partial x^2}\right) = -i\gamma g x \frac{\partial \vec{\mathbf{M}}}{\partial t} + D\frac{\partial^2}{\partial x^2}\left(\frac{\partial \vec{\mathbf{M}}}{\partial t}\right) \\ &= -(\gamma g x)^2 \vec{\mathbf{M}} - i2\gamma g x D\frac{\partial^2 \vec{\mathbf{M}}}{\partial x^2} + D^2\frac{\partial^4 \vec{\mathbf{M}}}{\partial x^4} - i2\gamma g D\frac{\partial \vec{\mathbf{M}}}{\partial x} \end{aligned} \qquad [3.31]$$

Substituting Eq.[3.31] into Eq.[3.30], the consistence error can be expressed as

$$\begin{aligned} E_{i}^{n} = 0.5\alpha\Delta x^2\left(s - \frac{1}{6}\right)\left[\frac{\partial^4 \vec{\mathbf{M}}}{\partial x^4}\right]_{i}^{n} + 0.5\Delta t\Big\{&-(\gamma x_i g^{n})^2 \vec{\mathbf{M}}_{i}^{n} \\ &-i2\gamma x_i g^{n} D\left[\frac{\partial^2 \vec{\mathbf{M}}}{\partial x^2}\right]_{i}^{n} - i2D\gamma g^{n}\left[\frac{\partial \vec{\mathbf{M}}}{\partial x}\right]_{i}^{n}\Big\} + O(\Delta t^2 + \Delta x^4) \end{aligned} \qquad [3.32]$$

The overall consistence error caused by the simulation is the sum of Eq.[3.32]

$$\begin{aligned} E^{n} &= \left|\sum_{i,n} E_{i}^{n}\right| \\ &= \left|\sum_{i,n}\left\{0.5\alpha\Delta x^2\left(s - \frac{1}{6}\right)\left[\frac{\partial^4 \vec{\mathbf{M}}}{\partial x^4}\right]_{i}^{n} - 0.5\Delta t(\gamma x_i g^{n})^2 \vec{\mathbf{M}}_{i}^{n} - iD\gamma g^{n}\Delta t\left[\frac{\partial \vec{\mathbf{M}}}{\partial x}\right]_{i}^{n} + O(\Delta t^2 + \Delta x^4)\right\}\right| \end{aligned} \qquad [3.33]$$

Hence, the consistency error for the Bloch-Torrey equation not only depends on the jump probability, *s*, but also depends on the amplitude of the gradient, *g*, the spatial step size, Δx, and

the size of the computational domain.

3.5.2 Computational Error

Section 3.5.1 shows errors are dependent on diffusion-sensitizing gradients. In practice, a dimensionless factor β is defined to evaluate the influence of this effect of gradients, namely,

$$\beta = Q \cdot \Delta x / \pi \qquad [3.34]$$

where

$$Q = \max\{f(t)\},\ f(t) = \int_0^t g(t')dt' \qquad [3.35]$$

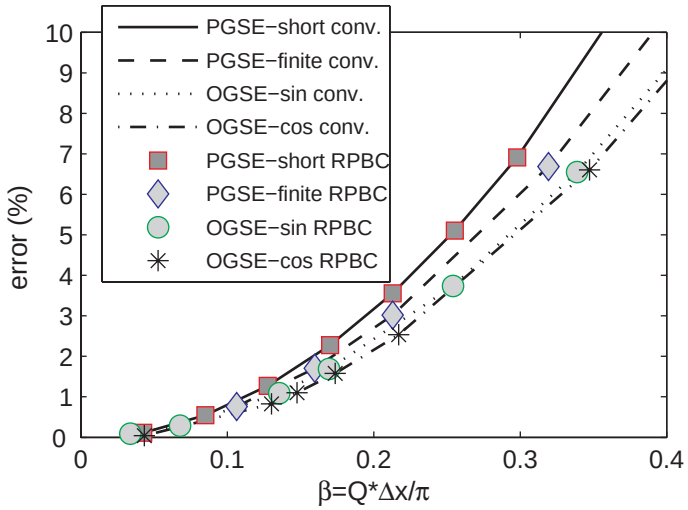

Fig. 3-8 Simulation errors change with respect to a dimensionless factor $\beta = Q^*\Delta x/\pi$. The results of conventional FD method were taken from the central region unaffected by the edge effect.

Fig. 3-8 shows that both conventional FD and the improved FD method with RPBC have increasing simulation errors with the amplitude of gradient increasing. Furthermore, both FD methods show the same behavior with respect to β (noting that results of conventional FD method were only taken from the central region unaffected by the edge effect) which implies this might be an intrinsic property when the FD algorithm is used to solve the Bloch-Torrey equation. In practice, $\beta < 0.1$ is needed to obtain a simulation error smaller than 1%.

3.6 Simulations of Comparing Two FD Methods

3.6.1 Isotropic diffusion

To test the feasibility of our method, diffusion in a 1D sample of isotropic diffusion was simulated first. Four types of diffusion-weighted pulse sequences were used: the pulse gradient spin echo (PGSE) with short gradient approximation (PGSE-short) (31), PGSE with finite duration of gradients (PGSE-finite) (43), oscillating gradient spin echo (OGSE) with sine-modulated gradient waveforms (OGSE-sin) and OGSE with cosine-modulated waveforms (OGSE-cos) (34,49). The parameters used were: diffusion coefficient D = 1 μm^2/ms, b = 1 ms/μm^2, Δx = 0.2 μm, Δt = 10^{-3} ms and total number of grid points N = 201 for all sequences; time between the onsets of two gradients Δ = TE/2 for both PGSE sequences; duration of gradient δ = 10^{-3} ms for PGSE-short, δ = Δ/2 for PGSE-finite and both OGSE sequences; frequency of the applied oscillating gradient f = 4/δ, i.e. 320Hz – 16kHz for TE = 1-50 ms.

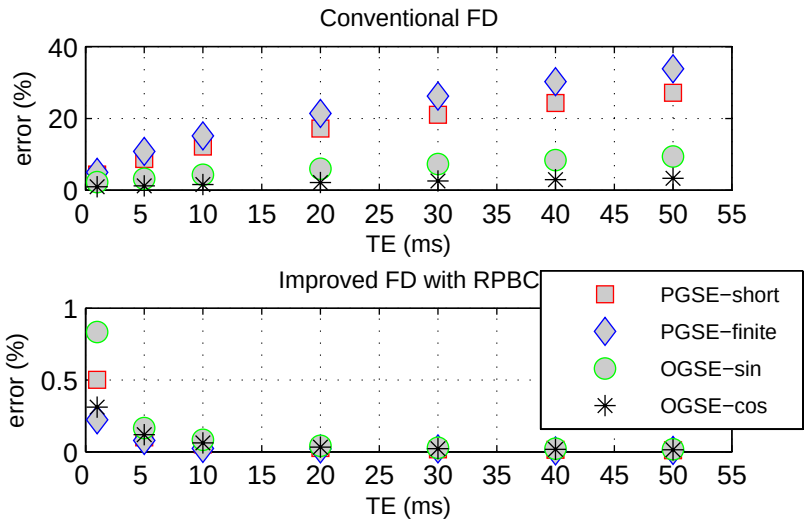

Fig. 3-9 Comparison of conventional FD and improved FD with RPBC for 1D isotropic diffusion sample with four types of pulse sequences.

Fig. 3-9 shows a comparison of the conventional FD and improved FD with RPBC methods for 1D isotropic diffusion with four types of pulse sequences: PGSE-short, PGSE-finite, OGSE-sin and OGSE-cos (definitions see above). Note that results with the conventional FD method are

calculated from the whole computational domain and show large errors caused by the edge effect. The conventional FD gives larger errors when TE increases which shows the significant influence of the edge effect. In contrast, the errors of the improved FD with RPBC are all smaller than 1% for all pulse sequences and diffusion times which confirms that the edge effect has been removed by the use of RPBC. One interesting feature is that both OGSE sequences give much smaller errors than the PGSE for conventional FD method which shows the barrier-induced effect has been reduced. This may be explained in terms of the relatively smaller effective diffusion time obtained by the OGSE (37). The definition of error is the same as Fig. 3-4.

3.6.2 Hexagonal Array of Permeable Cylinders

Some neural tissues, such as white matter, are often modeled as a bunch of parallel cylinders for studying water diffusion. Exact expressions for the ADC have been published for a single cylinder with impermeable walls (30) and with wall relaxation (31). An analytical expression for the thermal conductivity has been obtained for hexagonal arrays of perfectly conducting cylinders (50). Thermal conductivity and diffusion are analogous transport properties, so an analytical expression for the transverse ADC of hexagonal arrays of cylinders with perfect diffusivities at the cylinder boundaries may be obtained as (39)

$$ADC(\Delta \to \infty) = D_e \left[1 - 2f \left(\xi + f - \frac{0.075422 f^6 \xi}{\xi^2 - 1.060283 f^{12}} - \frac{0.000076 f^{12}}{\xi} \right)^{-1} \right], \quad [3.36]$$

where

$$\xi = (1+\kappa)/(1-\kappa), \quad \kappa = D_i / D_e \quad [3.37]$$

and D_i, D_e are diffusion coefficients inside the cylinders (intra-cellular space) and outside the cylinders (extra-cellular space), respectively, and f is the volume fraction of cylinders.

Fig. 3-10 shows the cross-section of a hexagonal array of cylinders simulating white matter axons. Cylinders (grey in Fig. 3-10) are axons and the surrounding matrix (white) is extra-cellular space. To compare with the analytical results, the myelin was assumed to be non-space occupying and with infinite permeability, and the diffusion time is very long (TE = 50ms). The conventional FD

method should simulate a much larger image to avoid the edge effect, whereas the improved FD with RPBC only needs to simulate the smallest unit cell of the structure.

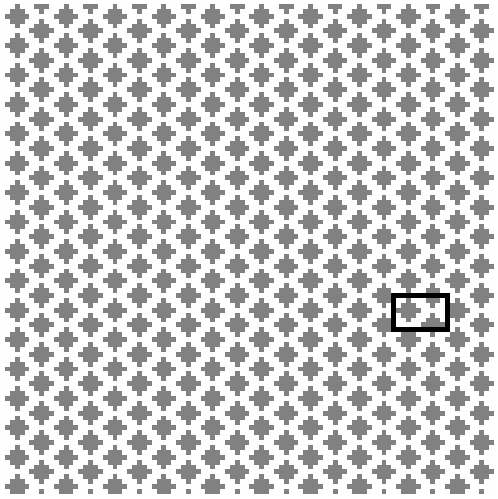

Fig. 3-10 Cross-section of a hexagonal array of cylinders: cylinders are grey and the surrounding matrix is white. To avoid the edge effect, the conventional FD method simulates the whole image and takes signals from the central barely affected domain for long diffusion times; whereas the improved FD method with RPBC only needs to simulate a unit cell (in the black box).

Simulated and analytical results for structures with different cylinder volume fractions are compared in Fig. 3-11. The sizes of cylinders were kept constant so that the change of interspacing of cylinders yields the various volume fractions. A PGSE-short pulse sequence was used in the simulations with parameters: D_i = 1.12 μm^2/ms, D_e = 1.65 μm^2/ms, $\Delta x = \Delta y$ = 0.5 μm, TE = 50 ms and number of points $N_x = N_y$ = 96 for the whole image.

Fig. 3-11 shows again the large errors caused by the edge effect (26% - 32%). It seems taking results only from the central unaffected computational domain (39) did remove the edge effect for the conventional FD method. However, it is much less efficient that 88% (2D) or 96% (3D) of the computational domain (and thus the computing time) was actually *wasted*. In contrast, the improved FD with RPBC gave relatively accurate results but was much more efficient (less than 5% of the computing time of the conventional FD method in the simulations of Fig. 3-11).

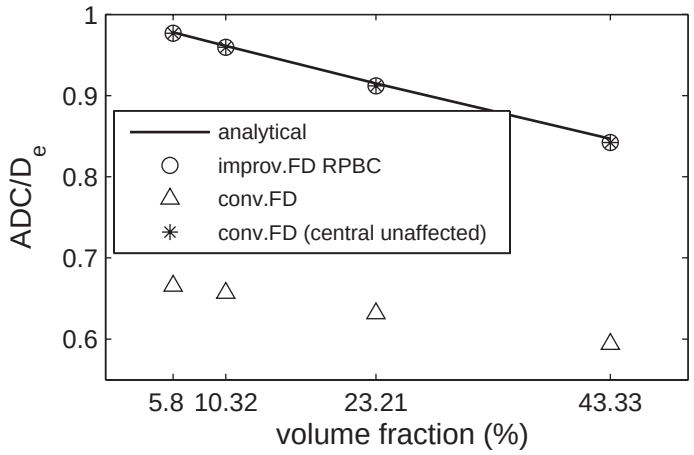

Fig. 3-11 Comparison of simulated and analytical results for hexagonal array of cylinders. For conventional FD, the results were taken from both whole domain and central unaffected domain for comparison.

3.6.3 Cubic Cells on a Cubic Grid

It has been reported that ADC in brain tissue drops significantly soon after the onset of a stroke (10,51). It has also been shown that ADC changes with intra-cellular volume fraction (52). Hence, the relationship between ADC and intra-cellular volume fraction is of considerable interest. Two analytical expressions for the ADC for cubic cells on a cubic grid have been developed using two types of models: parallel-series (PS) and series-parallel (SP) (38). For a cubic cell with size of L and permeability P_m on a cubic grid, the ADC expressions are

$$ADC^{PS}(\Delta \to \infty) = \frac{f^{2/3}}{\dfrac{f^{1/3}}{D_c} + \dfrac{1-f^{1/3}}{D_e}} + (1-f^{2/3})D_e \qquad [3.38]$$

$$ADC^{SP}(\Delta \to \infty) = \left[\frac{f^{1/3}}{f^{2/3}D_c + (1-f^{2/3})D_e} + \frac{(1-f^{1/3})}{D_e} \right]^{-1} \qquad [3.39]$$

where D_c is the effective ADC for a cell

$$D_c = \left[\frac{2}{P_m L} + \frac{1}{D_i} \right]^{-1} \qquad [3.40]$$

Simulated results for such an array using the improved FD method with RPBC are shown in Fig. 3-12. The parameters used the measured values for red blood cells: D_i = 0.63 μm^2/ms, D_e = 2 μm^2/ms and P_m = 0.024 μm/ms (52) and the others are same in above sections.

The simulated results match the PS model quite well, better than the SP model. This might imply that the PS model is more accurate for packed red blood cells which is consistent with previous experiments (52). The simulations using the conventional FD method were not performed here because it requires thousands of times more computing time, whereas the improved FD with RPBC method took only seconds to run.

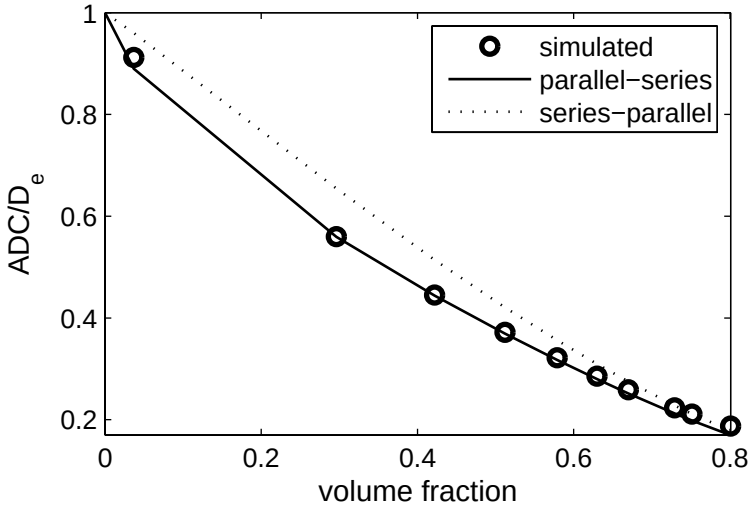

Fig. 3-12 ADC changes with respect to the intra-cellular volume fraction for a diffusion system of cubic cells on a cubic grid. Simulated results show good agreement with the PS model which is consistent with the experimental data on packed red blood cells.

3.6.4 Large-scale Sample of Pure Water

Although the improved FD with RPBC algorithm significantly reduces the effective dimensions of a tissue sample and, hence, increases the computing efficiency, heterogeneous tissue samples are usually very complicated and have large dimensions, especially for a simulation with sub-cellular resolution. High performance computing may be used to address such a large-scale computing problem. To test the computing performance of our tightly-coupled parallel computing

model, a large sample of pure water with a 101×101×101 grid was simulated using different number of processors using PGSE-short pulse sequence. The parameters used were D = 2.5 μm^2/ms, b = 1 ms/μm^2, temporal interval Δt = 0.001 ms, spatial interval Δx = 0.5 μm, TE = 100 ms and the size of computational domain along one direction = 2a, a = 50 μm.

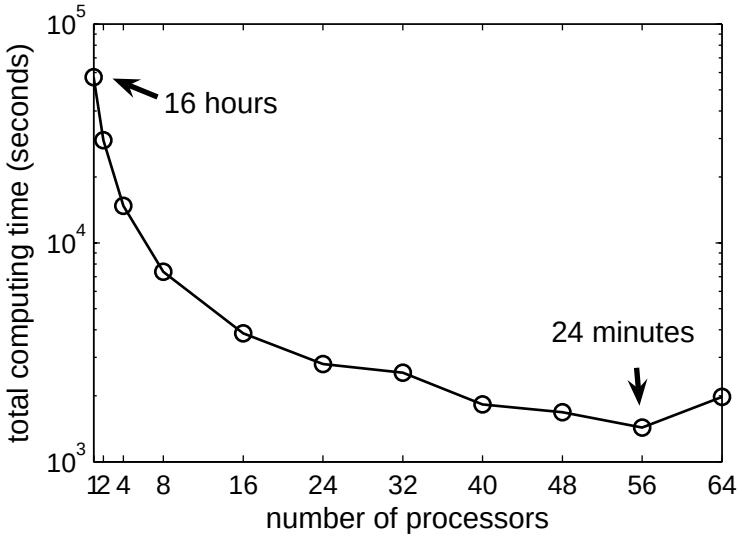

Fig. 3-13 Total computing time changing with respect to the number of processors. Total computing time includes the processor execution time, communication and synchronization time.

Fig. 3-13 shows the total computing time decreases as more processors are used. The total computing time for 56 processors is only 2.5% of the time for a single processor. The advantage of using parallel computing is obvious. Note that the total computing time reaches its minimum when 56 processors were used in the simulation while the computing time increases when more (64 shown in Fig. 3-13) processors are used. The reason is that when more processors are used in the simulation, the communication and synchronization time spent among the processors increases. When the portion of the communication time is too large, the computing time begins to increase again and the efficiency of parallel computing decreases. This shows that, for a certain problem, the parallel computing technique can not decrease the total computing time indefinitely as more processors are used. There is a minimum computing time for a specific problem with specific computing facilities.

To better understand the parallel computing performance of our model, a speed chart is plotted in Fig. 3-14. Speedup is defined as $S = t_1 / t_n$, t_1 is the computing time for a sequential program (one processor) and t_n is the total computing time for n processors. Our result reaches the ideal (theoretical maximum) speedup for up to 16 processors and performance still increases when less than 56 processors are used, which verifies computing performance of the tightly-coupled parallel computing model. The speedup drops down as more time is spent on communication and synchronization which means the parallel computing performance decreases.

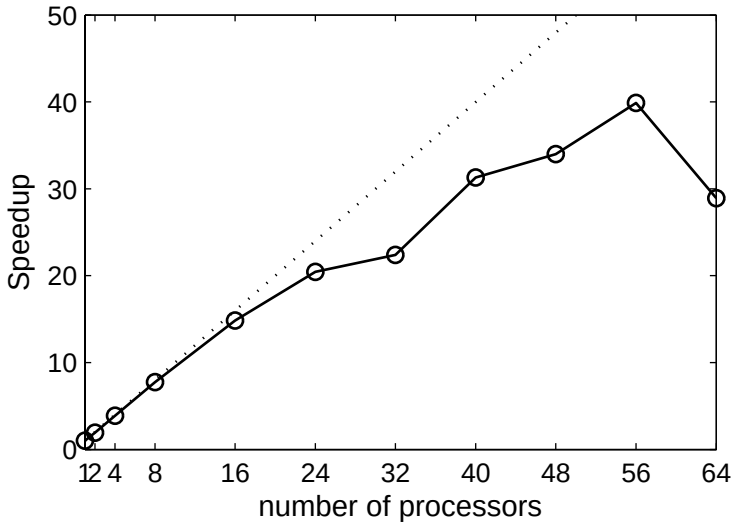

Fig. 3-14 Speedup chart of tightly-coupled parallel computing model.

3.7 Conclusion

The MC method is time consuming for complex tissues because it must track a large number of spins which encounter boundaries in the simulation in order to retrieve structural information. In contrast, the FD method determines the spin migration probabilities at the start of the simulation, which must therefore already contain tissue structural information. Thus, FD is usually computationally more efficient. This chapter introduces an improved finite difference method, which not only eliminates the edge effect induced by the conventional FD approach but also enables the efficient large-scale simulation of diffusion in biological tissues with the implementation of a tight-coupled parallel computing model. This method is applicable to studies

of water diffusion in MRI to aid the interpretation of diffusion-weighted imaging measures and their dependence of the morphology of biological tissues such as tumors.

CHAPTER IV

DWI SIGNAL MODELING AND DATA INTERPRETATION

Tissue structural information is important in both clinically and in research applications. For example, measurements of tumor cell nuclear size have been suggested as a biomarker for tumor detection and grading (53,54) while the size of axons reflects structure in while matter and affects axon conduction properties (55,56). Usually, histological information may only be obtained from invasive biopsies. Since diffusion-weighted magnetic resonance imaging (DWI) is dependent on the microstructural properties of biological tissues, it is possible to noninvasively obtain quantitative structural information from DWI measurements. However, to interpret the data an appropriate tissue model is needed.

Among various tissue modeling approaches, treating diffusion curves with a bi-exponential function is a common model to interpret DWI data. However, attempts to correlate the fitted parameters from the bi-exponential model to real biological tissue parameters have failed and the discrepancy between fitted and real data remains unsolved. Section 4.1 studies the bi-exponential model and reveals the origin of bi-exponential diffusion behavior may not be the existence of two diffusion compartments (intra- and extra-cellular space) but shows that any diffusion restriction can cause a bi-exponential diffusion behavior.

Oscillating gradient spin echo (OGSE) method may probe short diffusion times and, hence, have the potential to detect changes over much shorter length-scales which usually cannot be obtained with PGSE method. Section 4.2 investigates appropriate tissue models and data interpretation with OGSE based on the theory of temporal diffusion spectroscopy. The developed models fit both experimental and simulated data well and extract quantitative tissue microstructural information.

4.1 The Illusion of Bi-Exponentials: Apparent Compartmentalization in Diffusion MRI

4.1.1 Introduction of Bi-Exponential Model

Non-mono-exponential diffusion-induced MR signal decay has long been reported in cell aggregates (57) in tissues, in small animals (58) and human subjects (59). In addition, the non-mono-exponential decay usually can be well fitted to a bi-exponential function, i.e.

$$S(b)/S_0 = f\exp(-bD_{slow}) + (1-f)\exp(-bD_{fast}), \qquad [4.1]$$

where $S(b)$ and S_0 are the MR signals with and without diffusion-sensitizing gradients, b is the conventional gradient factor, f the fraction of the magnetization associated with the slow diffusion rate D_{slow}, and D_{fast} the higher apparent diffusion rate for the remainder. Eq.[4.1] has been interpreted as evidence of two separate compartments with different intrinsic properties between which the water exchange is assumed to be intermediate or slow. Experimental data often fit this model well and bi-exponential parameters have been assessed and interpreted in several applications, such as the characterization of brain tumors (60), adult and newborn brains (61), early stages of ischemic stroke (62) and the response of tumors to treatment (63). However, the origin of this so-called bi-exponential diffusion behavior remains unclear. Attempts have commonly been made to correlate the bi-exponential diffusion to actual water compartments, and some appear to interpret the fitted slow and fast diffusion components as directly representing the intra- and extracellular water in tissues. However, the apparent slow and fast volume fractions obtained from bi-exponential diffusion data fits differ significantly from intra- and extracellular volume fractions estimated from histology, and, in addition, differ from those obtained by hybrid diffusion experiments which incorporate other MRI contrast mechanisms such as T_2 (64-66).

There are several possible reasons to explain these discrepancies, such as differences in relaxation times of intra- and extracellular compartments, or faster water exchange between those compartments, but some potential explanations have been shown to not be adequate. For example, it was observed by Niendorf *et al.* (67) that the obtained volume fractions from bi-exponential fitting were independent of TE, which implies that T_2 differences cannot explain the discrepncy.

Mulkern *et al.* used inversion pulses with a range of inversion times of 40-500 milliseconds and found no statistically significant difference in the T_1 values of the fast and slow diffusion compartments in both cortical gray matter and the internal capsule of the human brain (68). Clark and Le Bihan measured the anisotropy of the apparent volume fractions using high b-value diffusion measurements of human brain (69). Sehy *et al.* obtained both slow and fast diffusion components from the intracellular space alone (70) while Grant *et al.* observed bi-exponential diffusion behavior in sub-cellular compartments, including the nucleus and cytoplasm in a large neuronal cell (71). Schwarcz et al. found bi-exponential diffusion behavior in a cold injured tissue in which cell membranes have disintegrated (72). Sukstanskii *et al.* studied a single cell-like compartment by simulation and found the impermeable barrier made the magnetization inhomogeneous with a short diffusion time, leading to a non-mono-exponential signal decay which can be fitted well by a bi-exponential model (73). Kiselev and Il'yasov questioned whether the high accuracy of data fitting to the bi-exponential model necessarily implies the presence of two distinct compartments (74).

4.1.2 Diffusion Restriction and Apparent Compartmentalization from Bi-Exponential

Diffusion rates in tissues are substantially lower than in homogeneous protein solutions, and the presence of restricting membranes or surfaces is important to explain such differences. Diffusion in restricted geometries can by itself give rise to non-monoexponential signal decays, as has been known for many years (75) but this potential contribution to bi-exponential decays continues to be overlooked. Numerical simulations have been used before to predict bi-exponential diffusion, e.g. Chin *et al.* used computer simulations to predict bi-exponential diffusion based on histological images from a rat spinal cord region (40). To further emphasize the role of restrictions in shaping the decay curves of water in compartmental systems, and to help interpret the experimental data obtained from tissues, we have used an improved finite difference method to study the diffusion behavior of a simplified 3D model corresponding to packed cells separated from the bulk medium by membranes of finite permeability. By assuming all other parameters are

homogeneous, including the proton density, T_1, T_2 and intrinsic diffusion coefficient, a good fit to bi-exponential diffusion behavior is still observed when the permeability is low, and the parameters obtained from a bi-exponential fit are dependent on the diffusion times, cell diameter and permeability. Furthermore, bi-exponential behavior is still observed with long diffusion times when there is no significant barrier-induced magnetization inhomogeneity. Thus, the bi-exponential diffusion behavior originates purely from the restriction on diffusion in this homogeneous system, and it is greatly affected by the water exchange rate and membrane permeability.

4.1.2.1 Methods

A 3D tissue model with packed cells

A simplified 3D two-compartment tissue model was used to simulate the behavior of water diffusion in tissues (see Fig. 4-1). The tissue is considered as a regularly packed system of filled spherical cells suspended in an extra-cellular fluid, and T_1, T_2, proton density and intrinsic diffusion coefficient are assumed homogeneous everywhere. Hence, there is only one intrinsic water pool in the model, although the whole tissue can be considered as two regions, the intra- and extra-cellular spaces, separated by cell membranes. The membranes are considered to be semi-permeable and results for three values of the permeability (= 0.001, 0.01 and 0.1 μm/ms) are provided below. Data are presented for two modeled tissues: tissue_I has cells of the size of 2 μm, which is more representative of cortical grey matter and the other one tissue_II has size of 10 μm cells which represents other tissues such as tumors. The intrinsic diffusion coefficient can be selected and results below are for the chosen values = 1 or 2 μm^2/ms everywhere for tissue_I and tissue_II respectively. The diameter and spacing of the cells are variable, but when they are close-packed the intra-cellular and extra-cellular volume fractions are 61.8% and 38.2% (for tissue_I) and 67.1% and 32.9% (for tissue_II), respectively. Tissue_I is discretized to a 30×30×30 matrix and tissue_II a 73×73×73 matrix.

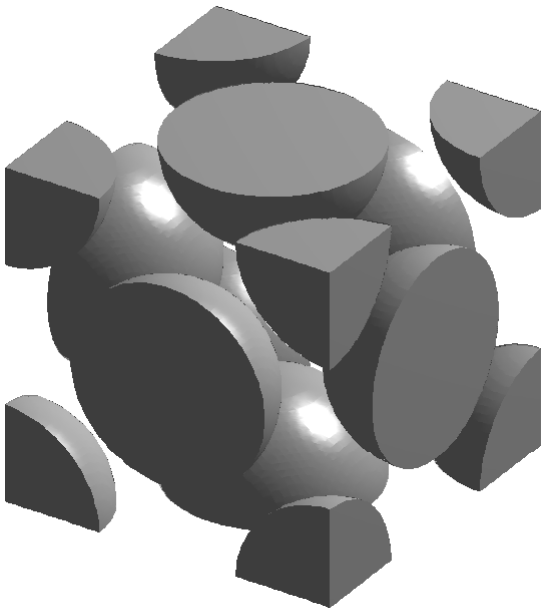

Fig. 4-1 A 3D tissue model with packed spherical cells and semi-permeable cell membranes.

In each simulation, the spatial steps for water molecules undergoing random diffusion were $\Delta x = \Delta y = \Delta z = 0.2$ μm and the temporal increment used was $\Delta t = 1$ μs. Simulations were performed with 8 Opteron processors (2.0 GHz) on the computing cluster of the Vanderbilt University Advanced Computing Center for Research & Education. The programs were written in C (GCC 4.1.2) with message passing interface (MPICH2) running on a 64-bit Linux operation system with a Gigabit Ethernet network.

All signal decays were fitted to Eq.[4.1] using a non-linear least-squares Levenberg-Marquardt algorithm provided by the optimization toolbox of Matlab (Mathworks, Natick, MA). The quality of fitting was evaluated by χ^2, the square 2-norm of the residuals.

4.1.2.2 Apparent Compartmentalization Dependent on Diffusion Time

Fig. 4-2(a) shows that when the cells are relatively small (2 microns) D_{slow} increases from 0.02 $\mu m^2/ms$ at $\Delta = 4$ ms to 0.16 $\mu m^2/ms$ at $\Delta = 100$ms, whereas D_{fast} is 0.78 $\mu m^2/ms$ at $\Delta = 4$ ms and decreases gradually down to 0.59 $\mu m^2/ms$ at $\Delta = 100$ ms. Fig. 4-2(b) shows how f, the fitted volume fraction of the "slowly diffusing" compartment changes with the diffusion time. f is

56.2% at Δ = 4ms and monotonically decreases to 28.5% at Δ = 100 ms. All data fitting have reasonably small errors ($\chi^2 < 10^{-5}$) which shows the bi-exponential fits the data very well. Note that the diffusion time only goes down to only 4 ms in the simulations because of the simulation error consideration. As the diffusion time decreases, in order to interrogate a large range of b values to explore the bi-exponential characteristics, larger amplitudes of gradient must be applied but at very short diffusion times this can cause larger simulation errors in the simulation (48).

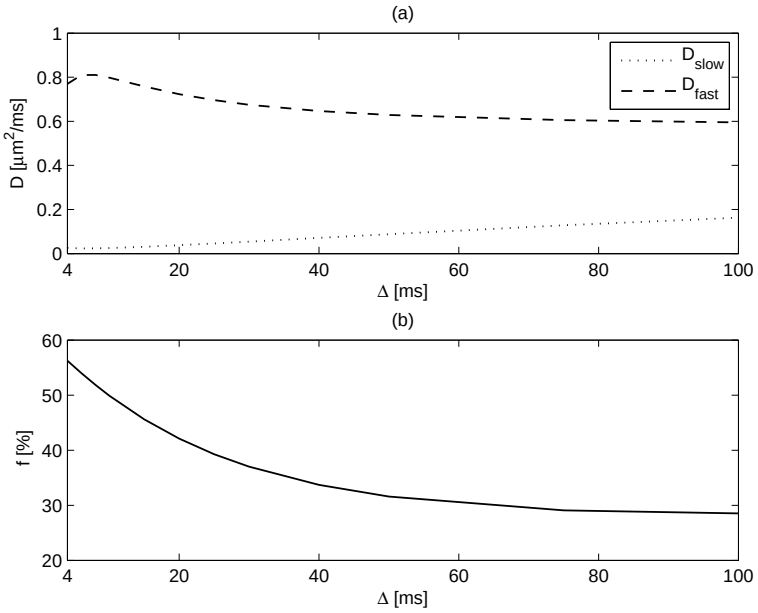

Fig. 4-2 Fitted parameters obtained from a bi-exponential data fitting change with diffusion time for tissue_I (a) fitted slow and fast diffusion coefficients and (b) the fitted volume fraction of slow diffusion component.

Fig. 4-3(a) shows that when the cells are large (10 microns) D_{slow} increases from 0.85 μm^2/ms at Δ = 6 ms to 0.16 μm^2/ms at Δ = 100ms, whereas D_{fast} is 3.49 μm^2/ms at Δ = 6 ms and decreases gradually down to 1.41 μm^2/ms at Δ = 100 ms. Fig. 4-3(b) shows how f, the fitted volume fraction of the "slowly diffusing" compartment changes with the diffusion time. f is 89.1% at Δ = 6 ms and monotonically decreases to 43.7% at Δ = 100 ms. All data fits have reasonably small errors ($\chi^2 < 10^{-5}$). As for Fig. 4-2, the fitted D_{slow}, D_{fast} and f are all dependent on diffusion times.

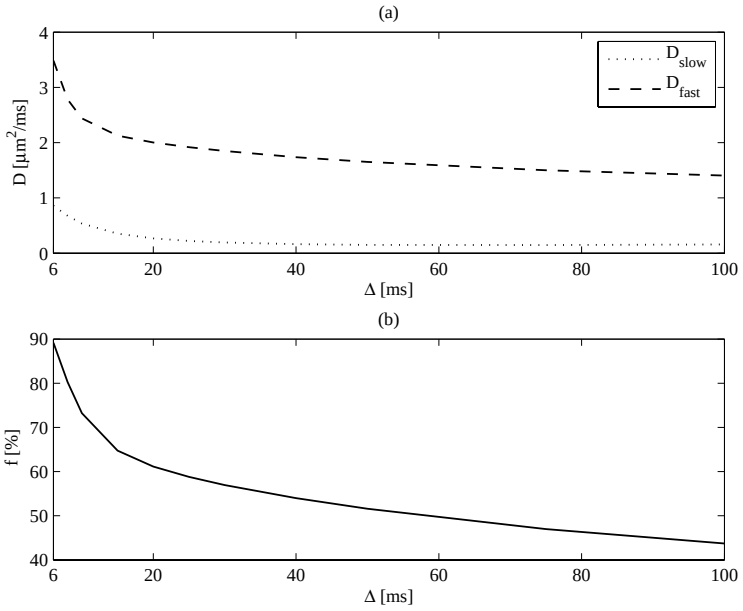

Fig. 4-3 Fitted parameters obtained from a bi-exponential data fitting change with diffusion time for tissue_II (a) fitted slow and fast diffusion coefficients and (b) the fitted volume fraction of slow diffusion component.

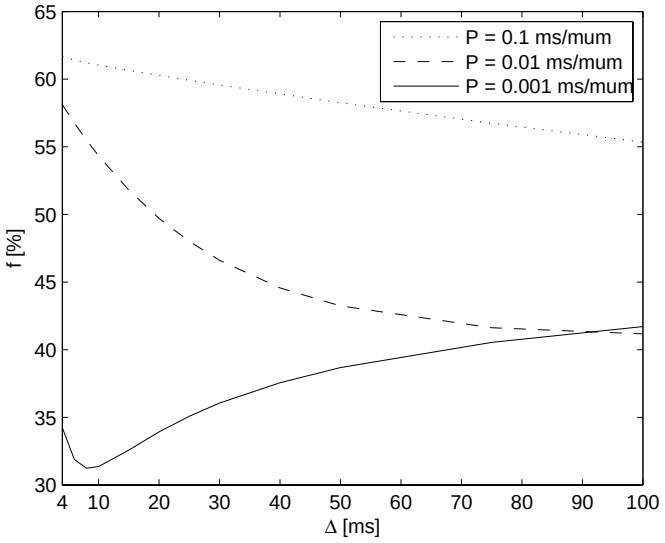

Fig. 4-4 The fitted volume fraction of slow diffusion component change with diffusion times and membrane permeabilities.

Fig. 4-4 shows how the fitted volume fraction of the slow diffusion compartment changes with

different diffusion times and membrane permeability for tissue_I. When the permeability is low (= 0.001ms/μm) the water exchange between intra- and extra-cellular space is slow, and f monotonically decreases from 61.4% at Δ=4ms to 53.4% at Δ=100ms, whereas when the permeability is much higher (= 0.1ms/μm) and water exchange is fast, f decreases from 34.2% at Δ=6ms to 31.4% at Δ=8ms and then increases to 41.7% at Δ=100ms.

To further study the apparent "compartmentalization", the standard deviation of the magnetization distribution of tissue_I at the echo time (STD shown in Fig. 4-5) was plotted versus diffusion time in Fig. 4-5. All curves were obtained with b = 4ms/μm^2. The STD decreases with increasing diffusion time which means the magnetization becomes more homogeneous with a longer diffusion time. With an intermediate water exchange rate (P=0.01ms/μm), the magnetization approaches homogeneous when Δ>50ms. For a relatively large water exchange rate (P=0.1ms/μm), the magnetization becomes homogeneous when Δ>50ms. If the magnetization is homogeneous, apparently, the compartmentalization of intra- and extracellular spaces becomes invalid. However, the bi-exponential diffusion behavior is still observed with long diffusion times.

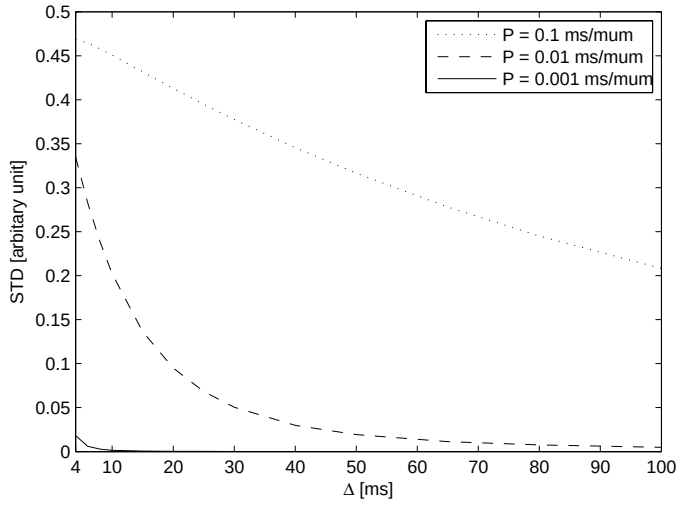

Fig. 4-5 Standard deviation of magnetization distribution at the echo time is dependent on diffusion time. Cell size is 2μm and b = 4 ms/μm^2.

4.1.3 Discussion

By making proton density, T_1, T_2 and the intrinsic diffusion coefficient everywhere uniform, and removing any intracellular structures, we exclude some possible causes of bi-exponential diffusion in our model. However, pronounced apparent bi-exponential diffusion behavior was still observed for the integrated water signal, and this can be entirely attributed to the effects of restricted diffusion due to the finite permeability of the membranes. Moreover, D_{slow}, D_{fast} and f change with diffusion time. A similar dependence has been reported by Thelwall *et al.* in their study of human erythrocytes, and they addressed this dependence on diffusion time due to the exchange between intra- and extracellular water (76). In our simulations, the water exchange between intra- and extracellular spaces was observed to influence the bi-exponential parameters. f, the fitted volume fraction of the slow compartment, decreases with diffusion time with a moderate permeability of 0.01 μm/ms. For a larger permeability 0.1 μm/ms, f decreases with diffusion time first and then increases because fast exchange of water contributes to homogenize the magnetization, making the whole signal decay mono-exponential.

Our simulation is based on a simple but realistic tissue model, which contains both intra- and extracellular spaces and semi-permeable membranes. The simulated results show that all diffusion MR signal decays have a bi-exponential behavior, and the fitted parameters depend on the diffusion time. With semi-permeable membranes and long diffusion times, the magnetization becomes homogeneous and the intra- and extracellular compartmentalization becomes invalid. The bi-exponential diffusion behavior with the conditions considered shows that the slow and fast diffusion components are illusory, and do not correspond to identifiable intra- and extra-cellular compartments. This may explain some previous discrepancies between fitted volume fractions and those obtained by histological analysis.

4.2 DWI Signal Modeling and Data Interpretation with Temporal Diffusion Spectroscopy

The oscillating gradient spin echo (OGSE) method has many advantages compared with the pulsed gradient spin echo (PGSE) approach, such as the ability to probe short diffusion time

behavior. However, due to the relatively complicated gradient waveforms, it is difficult to model MR signals with OGSE. In section 2.2.2 , the analytical expressions of MR signals with OGSE have been introduced and this makes it possible to model MR signals of complicated biological tissues and, hence, makes it possible to extract novel tissue structural information from biological tissues with the OGSE method. For example, it has been reported that cell division is closely related to cell size. For some cells, there is a mechanism by which cell division is not initiated until a cell has reached a certain size (77). Hence, cell size is important in tumor grading and has important application in cancer diagnosis. Usually, cell sizes can only be obtained from an invasive biopsy. With the analytical expressions of MR signals with OGSE method introduced in section 2.2.2 , we are able to model the DWI signals obtained from biological tissues and obtain cell sizes non-invasively.

4.2.1 One Diffusion Compartment Model: Packed HeLa Cells

In this section, only a one compartment model is considered. More complicated multiple diffusion compartment models will be discussed in the next section.

Recall Eq.[2.27], which is the analytical expression for signal attenuation of OGSE-cos with restricted diffusion

$$\beta(2\tau) = 2(\gamma g)^2 \sum_k \frac{B_k a_k^2 D^2}{(a_k^2 D^2 + \omega^2)^2} \left\{ \frac{(a_k^2 D^2 + \omega^2)\sigma}{2 a_k D} - 1 + \exp(-a_k D\sigma) + \exp(-a_k D\tau)(1 - \cosh(a_k D\sigma)) \right\}.$$

If cells are modeled as spherical structures, then B_k and a_k can be determined by Eq.[2.20], namely, $B_k = \frac{2(R/\mu_k)^2}{\mu_k^2 - 1}$ and $a_k = \left(\frac{\mu_k}{R}\right)^2$, where μ_k is the k^{th} root of equation $\mu J'_{3/2}(\mu) - \frac{1}{2} J_{3/2}(\mu) = 0$ (i.e. μ_k = 2.08, 5.94, 9.21, …) (36). Hence, a system with packed spherical cells, in which MR signals arise only from the intra-cellular space, can be modeled analytically with the equations shown above. In practice, the dispersion curve of ADC vs. gradient frequency is usually needed to tissue characterization. By substituting Eq.[2.21] and Eq.[2.27] into Eq.[1.13], one can obtain

$$ADC = \frac{2\varpi^2}{\sigma}\sum_k \frac{B_k a_k^2 D^2}{(a_k^2 D^2 + \omega^2)^2}\left\{\frac{(a_k^2 D^2 + \omega^2)\sigma}{2a_k D} - 1 + \exp(-a_k D\sigma) + \exp(-a_k D\tau)(1-\cosh(a_k D\sigma))\right\}$$

[4.2]

Eq.[4.2] shows the relationship of ADC obtained with OGSE method and the applied gradient frequency. Hence, if a dispersion curve (*ADC* vs. ω) is measured by the OGSE-cos method with known sequence parameters, it can then be fitted to Eq.[4.2] to obtained structural information such as cell size, from the structural dependent parameters B_k and a_k.

Two packed HeLa cell pullets were studied to illustrate this model experimentally. One was normal/healthy cells that grew to 90% cell density and the other one was prepared from cells without serum (plain DMEM media) for 24 hours. Then the cells were tripsinized, washed twice with PBS and then pelleted into 5mm NMR sample tubes.

Experiments were done on a Varian 4.7T scanner with a 10mm RF coil using a simple OGSE pulse sequence (collecting NMR signals from the whole sample without taking images). Duration of each gradient was fixed at 40ms and echo time was 100ms. 12 acquisitions were averaged to enhance the SNR.

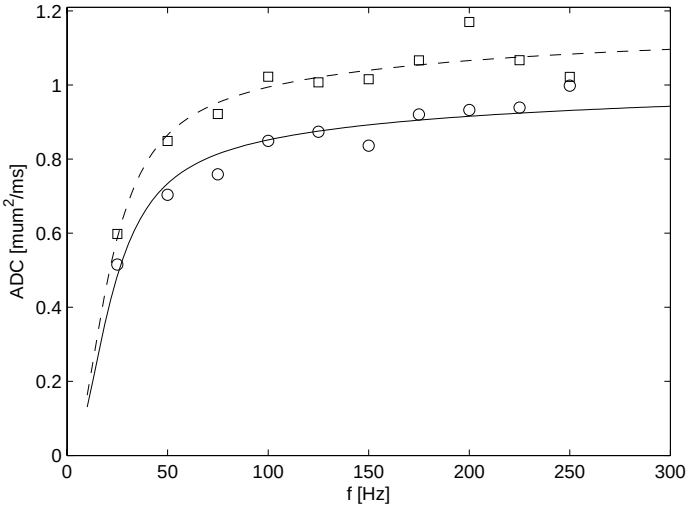

Fig. 4-6 Circles are experimental data for starving HeLa cells and squares for healthy HeLa cells. The solid and dashed lines are corresponding fitted curves, respectively.

For this packed cell sample, all MR signals can be considered from the intracellular space and, hence, it acts as a single diffusion compartment system. By fitting the experimental data to the analytical equations Eq.[4.2], we obtained the fitted results shown in Table 4-1.

Table 4-1 Fitted HeLa cell sizes and intra-cellular diffusion coefficients for packed HeLa cells, corresponding 95% confidence intervals included.

	mean HeLa cell diameter (μm)	intra-cellular D (μm^2/ms)
healthy HeLa cell	15.1±2.00	1.5±0.07
starving HeLa cell	16.8±2.25	1.6±0.08

The fitted mean HeLa cell diameter is close to the reported mean HeLa cell diameter, which is 14.6±1.7 μm (78). Hence, our model fits packed HeLa cells very well and are able to obtain structural information such as cell sizes, from the diffusion-weighted MR results with the OGSE method.

4.2.2 Two Diffusion Compartment Model with Slow Water Exchange

For many samples, the water exchange between two compartments i.e. intra- and extracellular spaces is slow (55). One example is the diffusion in axons. Diffusion inside the axon is called 'restricted' and the diffusion in the extra-cellular space is 'hindered'. We can model the total signal from such a tissue simply as a sum of the two components

$$E = \exp(-\beta(2\tau)) + \exp(-bD_{ex}), \qquad [4.3]$$

where 2τ is the echo time, β the signal attenuation of water inside cells/axons and D_{ex} the diffusion coefficient of extra-cellular space.

For the cylindrical array shown as below, we run the finite difference simulation using the method introduced in section 3.3 and then fit the simulated data into Eq.[4.3]. All used parameters are experimentally practical values, such as gradient amplitudes (11 values, ranging evenly from 0 to

100 G/cm) and three gradient frequencies (50 Hz, 100 Hz and 200 Hz) with TE = 40 ms.

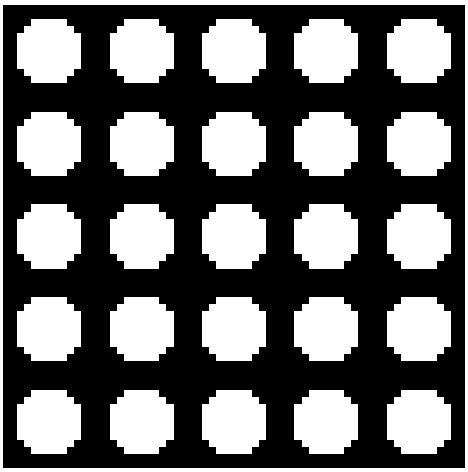

Fig. 4-7 Cross section of a cylindrical array used in the simulation. White region represents axons and black region extra-cellular space.

The fitted results and real values used in simulations are shown in Table 4-2, in which R is the radius of axon, D_{in} and D_{ex} are diffusion coefficients of axons and extra-cellular space, respectively. *frac* is the proton fraction of axons. Note that the fitted D_{in} gives accurate values with the absence of noise.

Table 4-2 Comparison of simulated structural parameters and fitted parameters with 95% confidence intervals.

	R (μm)	D_{in} (μm^2/ms)	D_{ex} (μm^2/ms)	*frac* (%)
real value	2.34	1.0	2.0	40.8
fitted value	2.42±0.02	0.97±0.04	1.37±0.03	44.1±1.00

Fig. 4-8 shows the simulated data of signal attenuation and the corresponding fitted curves. One can see that the data are fitted very well.

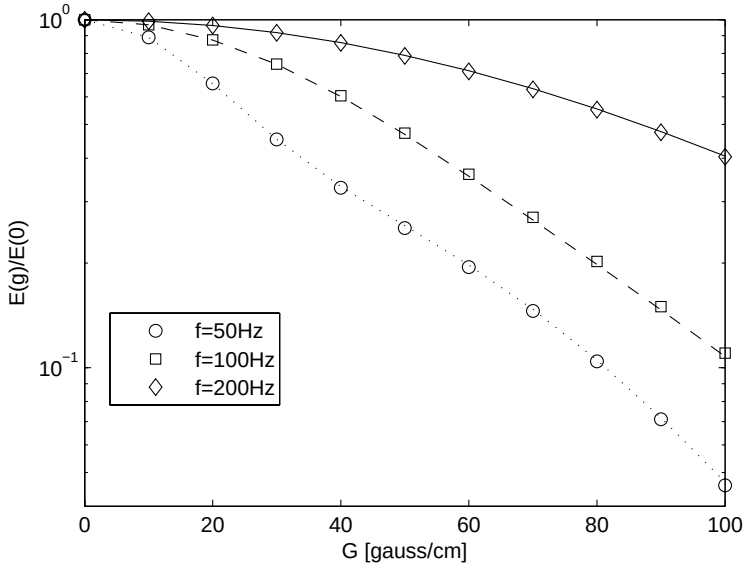

Fig. 4-8 Simulated data are shown as dots (f = 50 Hz), squares (100 Hz) and diamonds (200 Hz). Solid, dashed and dotted lines are corresponding fitted curves.

4.3 Conclusions

An improved finite difference simulation method has been used to study the so-called bi-exponential diffusion in a simple array of spherical compartments. Even without the influence of variations in other parameters, such as proton density, T_1, T_2 and intrinsic diffusion coefficient, bi-exponential diffusion decays are still observed. Results show that water exchange contributes significantly to the bi-exponential diffusion, but the main cause of the bi-exponential diffusion is restriction. In addition, the fitted parameters, such as the volume fraction of the slow diffusion compartment, are dependent on diffusion time. We confirm that the slow and fast diffusion components obtained from a bi-exponential data fitting may merely be apparent compartments due to the diffusion restriction and may not then correspond to identifiable intra- and extracellular compartments.

Besides the bi-exponential model, some other tissue models have been suggested to interpret DWI data and obtain tissue structural information. We introduced a new model method with the OGSE method, which employs relatively complicated diffusion-weighted gradient waveforms. The results show that this method can fit both the simulated and experimental data very well and

can provide tissue micro-structural information such as cell or axon sizes. This method provides a new insight into the biological tissue microstructures with diffusion temporal spectroscopy.

CHAPTER V

SENSITIVITY OF DIFFUSION MEASUREMENT TO VARIATIONS IN INTRACELLULAR STRUCTURES: EFFECTS OF NUCLEAR SIZE.

DWI can provide diagnostic insights into various pathologies such as stroke (10), and consequently has become an established clinical technique. In both animal and clinical studies, measurements of the apparent diffusion coefficient (ADC) of water have also been shown to provide information on the state of tumors and their response to treatments by revealing tissue characteristics such as tumor cellularity (23,24,79,80). Tumor cellularity is usually interpreted to mean cell density, though it may be measured histologically in terms of the integrated area of nuclei of cells divided by the total area of the histologic section. Regions with high cell density tend to have a lower ADC than regions with a low cellularity (79). This correlation makes ADC a potentially powerful biomarker for characterizing tumors and their early response to treatment. However, malignant tumors do not always have higher cellularities than normal tissues or benign tumors. For example, Guo *et al.* (81) found that a malignant scirrhous breast adenocarcinoma had a lower cellularity and elevated ADC compared to normal tissues, whereas a benign papilloma showed a higher cellularity and a lower ADC. Nonetheless, in these examples the inverse relationship of cellularity and ADC was conserved. This correlation in practice is actually a relationship between ADC and cell density. Conventional ADC measurements on MRI systems use the pulsed gradient spin echo (PGSE) method, in which gradients are applied in pairs, separated by a diffusion interval. Because of hardware limitations, and in order to impart sufficient diffusion weighting to be able to see significant signal reductions, the diffusion intervals used in practice are relatively long, typically several 10's of milliseconds (37). From the Einstein relationship, in a time of e.g. 40 ms, free water molecules with an intrinsic diffusion coefficient of 2.5×10^{-5} cm^2sec will move a distance on average ≈ 24 microns, which is larger than the dimension of most cells. The measured values of water ADC in many tissues are ≈ 5 times lower, suggesting that water diffusion in tissues is restricted. Such restrictions are caused,

for example, by structures such as cell membranes, which have limited permeability. Conventional measurements of ADC made using long diffusion intervals represent the integrated effects of obstructions to free diffusion at all scales up to the limiting value determined (as above) by the experimentally-selected diffusion interval. As such they may be dominated by obstructions at large scales, such as cell membranes, which reflect overall cell density, and they cannot distinguish these from restrictions that occur at smaller scales, such as those associated with intracellular structures. The observed relation between ADC and cellularity in conventional DWI measurements is likely a reflection of the effects of water molecules encountering different numbers of cell membranes in a specific time, and no separate information can be obtained about structural variations on sub-cellular scales. Although cell density may still be clinically useful as an indicator of tumor aggressiveness or metastatic capacity (82), it is plausible that more specific insights into tumor status may be provided by developing methods that are sensitive to intracellular properties.

Several authors have suggested that assessments of the sizes of tumor cell nuclei may be useful for diagnostic purposes (53,54). Indeed, nuclear anaplasia is a diagnostic feature of many malignancies and often represents the consequence of major changes in biochemical composition. A larger cell nuclear size usually means a more aggressive (high grade) tumor (83). In order to make diffusion measurements sensitive specifically to features such as nuclear size, they must be performed with diffusion times that are much shorter than those in common use. One approach to reduce diffusion times is the oscillating gradient spin echo (OGSE) method. The gradients commonly available on MRI systems can readily oscillate at frequencies of the order of a kilohertz, so that diffusion times can be achieved that are at least an order of magnitude shorter than with typical PGSE measurements. These in turn imply that OGSE measurements can be made much less sensitive to large scale restriction effects and thereby be more selectively sensitive to intracellular changes.

In the present work, the feasibility of using OGSE diffusion measurements to obtain information on cell nuclear sizes was evaluated numerically using an improved finite difference method to

simulate water diffusion within a 3D multi-compartment tissue model. The results show that conventional PGSE methods with typical choices of parameters can barely distinguish tissues with different nuclear sizes if the cell densities are the same, consistent with the view that conventional ADC measurements are dominated by cell density and are insensitive to intracellular structures. By contrast, the OGSE method can differentiate tissues with the same cell density but which differ over only very short length scales, which means the OGSE method can be much more sensitive to variations in intracellular structure such as nuclear sizes. Moreover, the simulations show that the degree of contrast produced by variations in ADC at high gradient frequencies (short diffusion times) that arise from variations in cell nuclear size are significantly greater than obtainable with PGSE methods. Thus OGSE measurements should prove more sensitive and specific for many purposes in their applications to tumor characterization. The effect of the choice of gradient amplitude in the OGSE method has also been studied, which can be helpful for selecting parameters in experimental applications.

5.1 A 3D Multi-Compartment Tissue Model

A simplified 3D multi-compartment model was used to simulate the behavior of water diffusing in tissues (see Fig. 5-1). The tissue is considered as a close-packed system of spherical cells. Each cell contains a central spherical nucleus. As a result, there are three distinct compartments containing water in this model, corresponding to intra-nuclear, cytoplasmic and extra-cellular spaces. Each component is ascribed its own intrinsic parameters, including a water self-diffusion coefficient and T_2. The interfaces between the compartments are assumed to be only semi-permeable and are each ascribed a value of permeability to water exchange. Mitochondria and other organelles are not explicitly modeled due to their small sizes. To include the averaged effect on diffusion due to restrictions and/or hindrance of organelles, the intrinsic diffusion coefficient of cytoplasm is given a value smaller than those of nucleus and extra-cellular space. This assumption has been confirmed by experimental observations (71).

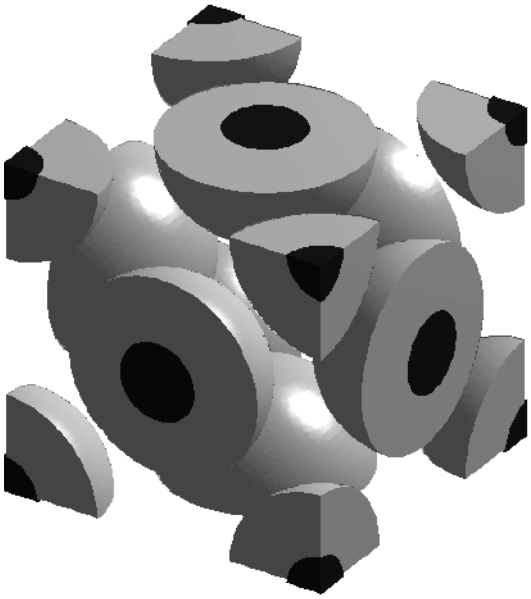

Fig. 5-1 Schematic diagram of a simplified 3D tissue model. Black regions represent cell nuclei, gray regions represent cytoplasm and the space outside the spherical cells are extracellular space. Each compartment has its own intrinsic parameters, such as diffusion coefficient. Interfaces between different compartments have permeabilities to mimic cell membranes and nuclear envelopes. Note that the whole tissue is periodic but only a unit cell (shown above) was needed in the simulation, which implemented a revised periodic boundary condition in an improved finite difference method.

The simulation can calculate the behavior of the ADC for a range of values of model parameters, but we here highlight only the results for realistic values relevant for MRI of tumors. We chose to simulate cells with diameters of 10 μm (typical of many human cells). For the results reported here, the cell size and spacing were kept constant but the nuclear size was varied so that the ratio of nuclear volume to cell volume (N/C) also varied.

All other simulation parameters were chosen from published experimental results: the cell membrane permeability was taken to be 0.024 μm/ms (52), the intrinsic diffusion coefficients for nucleus = 1.31 μm^2/ms, for cytoplasm = 0.48 μm^2/ms and for the extra-cellular space = 1.82 μm^2/ms (71). For all simulations, b = 1 ms/μm^2 and TE = 40 ms. T_2 was assumed homogeneous

everywhere.

In each simulation, the spatial steps for water molecules undergoing random diffusion were $\Delta x = \Delta y = \Delta z = 0.5$ μm and the temporal increment used was $\Delta t = 0.001$ ms. These parameters may be automatically adjusted in case of very high gradient amplitudes in order to keep all computational errors less than 1% (42). All simulations were performed on the computing cluster of the Vanderbilt University Advanced Computing Center for Research & Education. The programs were written in C with MPI (message passing interface) running on 2.0 GHz Opteron processors and a 32-bit Linux operation system with a Gigabit Ethernet network.

5.2 ADC Differences Obtained by PGSE and OGSE

Two types of tissue (denoted _I and _II) were simulated. They have the same structures except that the ratio N/C was different (and equals to 6.2% and 22.0%, respectively). The ADCs and percent difference in ADC (ΔADC) between the two tissues are shown in Fig. 5-2. On the left (Fig. 5-2a and Fig. 5-2c) are the results for the PGSE sequence as a function of diffusion time, and on the right (Fig. 5-2b and Fig. 5-2d) are the corresponding OGSE results as a function of gradient oscillation frequency. The shaded regions of Fig. 5-2c and Fig. 5-2d represent the typically relevant domains of diffusion time (20 – 80 ms) and oscillation frequencies (< 1 kHz).

Over these relevant domains, ADCs measured by PGSE are relatively constant, whereas, ADCs measured by OGSE change substantially. Similarly, ΔADC from PGSE measurements is small (< 3.6 %) and relatively insensitive to diffusion time, while ΔADC from OGSE measurements changes rapidly with increasing frequency and approaches 15 % at 1 kHz. That is, OGSE measurements in this model system reveal approximately 4 times greater percent difference in ADC between tissues that vary only in sub-cellular characteristics.

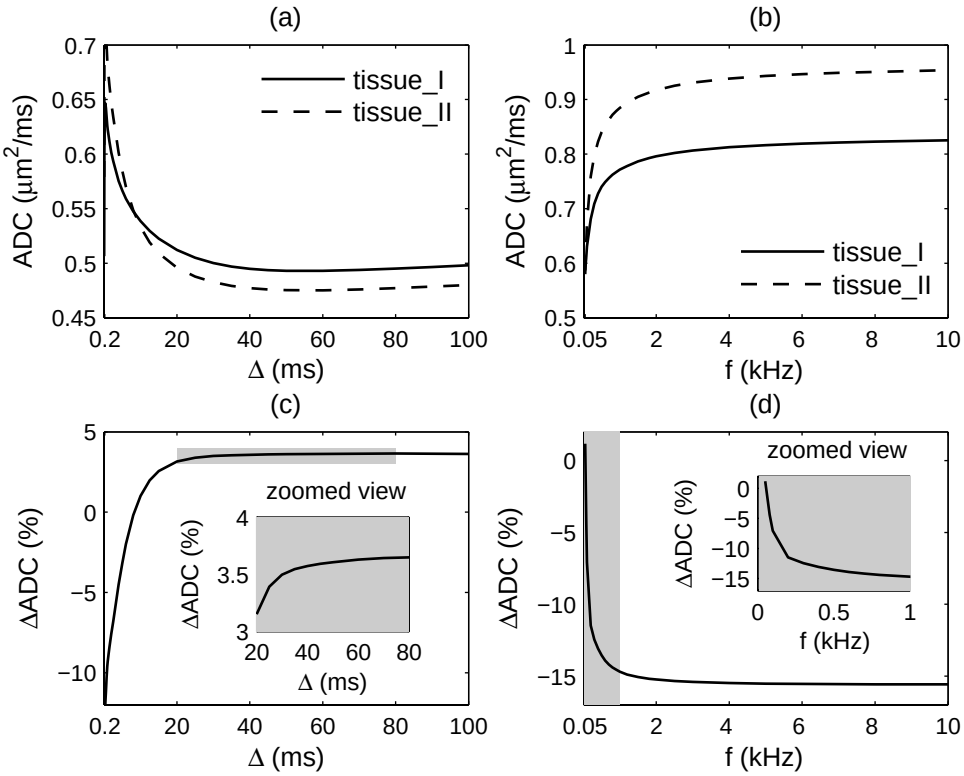

Fig. 5-2 Simulated ADCs and ADC differences of two different tissues (N/C 6.2% and 22.0%, respectively). (a) Simulated ADCs with respect to diffusion times by the PGSE method. (b) Simulated ADCs with respect to frequencies of applied oscillating gradients in the OGSE method. (c) ADC differences of two tissues by the PGSE method. The shaded region shows the applicable diffusion time range in typical PGSE measurements. (d) ADC differences of two tissues by the OGSE method. The shaded region shows the applicable oscillating gradient frequency range in typical OGSE measurements.

Fig. 5-2 also shows the interesting result that the ADC of tissue_II (with larger N/C) is larger than of tissue_I (smaller N/C) at short diffusion times, whereas it becomes smaller at longer diffusion times. At short diffusion times, the overall ADC approaches a weighted average of the intrinsic diffusion coefficients of each compartment. The intrinsic diffusion coefficient of water in the nucleus was assumed to be larger than the diffusion coefficient in the cytoplasm; hence, a larger N/C results in a larger ADC. At long diffusion times, water diffusion is heavily restricted/hindered

by membranes and the ADC will be lower when the average water molecules encounters more membranes. With the smaller nucleus, water in tissue_I is more likely to diffuse past the nucleus without encountering its membrane, thereby making the ADC in tissue_I higher than that in tissue_II.

5.3 ADCs Change with N/C Variation

The variation of tissue ADCs as a function of cell nuclear sizes is shown in Fig. 5-3. The solid line represents the ADCs obtained using the fast exchange approximation (all membranes are freely permeable), which can be considered as the tissue's mean intrinsic diffusion coefficient without any restriction. The dashed lines represent ADCs obtained by the OGSE method (at 200 Hz and 1 kHz). All ADCs obtained by the OGSE method are smaller than the corresponding intrinsic mean diffusion coefficients. The ADCs obtained by the PGSE method, shown as dotted lines in Fig. 5-3, show no notable changes over a broad range (from 2.9% to 73.7%) of variations of N/C, which is consistent with observation in Fig. 5-2 that typical PGSE methods are not sensitive to physical changes in tissue at the sub-cellular level. On the other hand, the OGSE-measured ADC changes smoothly and by ≈ 40 % over the same range of N/C, which means that the observations in Fig. 5-2 were not specific to a narrow range of N/C values. Also note the similarity between the OGSE curves in Fig. 5-3 and the solid line, which is simply a weighted average of the intrinsic compartment diffusion coefficients. This similarity points to the OGSE more closely measuring intrinsic diffusion coefficients rather than the effects of restrictions on the scale of 10s of μm apart.

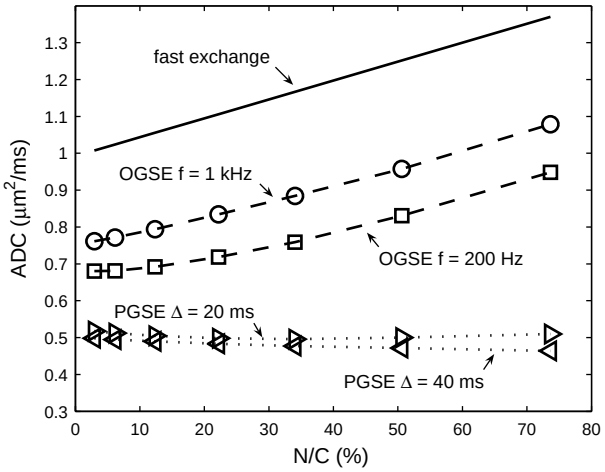

Fig. 5-3 Simulated ADCs change with the variation of N/C (the ratio of nuclear volume to cell volume). The solid line represents the ADCs with the fast exchange approximation. The dotted lines and dashed lines represent ADCs obtained by the PGSE method and OGSE methods, respectively.

5.4 Gradient Amplitude Limitation on OGSE Method

The data in Fig. 5-2 and Fig. 5-3 were derived using b = 1 ms/μm^2 at all frequencies, which can produce reasonable reductions in MRI signals to detect diffusion effects and permit accurate calculation of ADC values. However, in OGSE, b is proportional to $1/f^2$, and σ is limited by T_2 relaxation; hence, at high frequency it is difficult to achieve high b values with practical gradients. It is, therefore, of interest to assess limits on the OGSE method from constraints on gradient strength in order to help design practical experiments. Fig. 5-4 shows the maximum contrast between tissue_I and tissue_II in a diffusion weighted OGSE image (cosine gradients) for three different maximum gradient amplitudes. For comparison, the maximum contrast obtained by the PGSE method is also provided and shown as the solid line, assuming the conditions Δ = 40 ms and b = 1 ms/μm^2. The maximum contrast is defined as the absolute value of signal decay difference, namely,

$$\Delta S = \left| \exp(-b_{max} \cdot ADC_{\text{tissue\_I}}) - \exp(-b_{max} \cdot ADC_{\text{tissue\_II}}) \right|, \qquad [5.1]$$

where b_{max} is the maximum applicable b value for the measurements, and both b_{max} and ADC are gradient frequency dependent in the OGSE method.

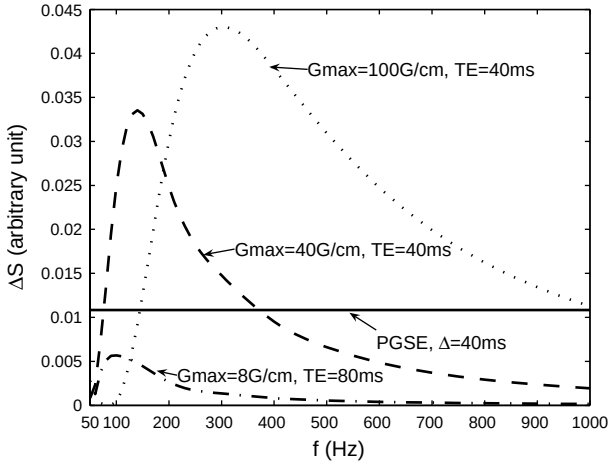

Fig. 5-4 Maximum contrast for the OGSE method between tissue_I and tissue_II as a function of gradient frequency in three typical cases. G_{max} is the gradient amplitude. The dashed line denotes the conditions for studies on small animal scanners with G_{max} = 100 G/cm and TE = 40 ms; the dotted line represents diffusion studies with G_{max} = 40 G/cm and TE = 40 ms; the dash-dot line depicts the conditions for *in vivo* diffusion studies on human scanners with G_{max} = 8 G/cm and TE = 80 ms. For comparison, signal contrast obtained by the PGSE method at Δ = 40 ms and b = 1 ms/μm^2 is also showed as the solid line.

The dotted line in Fig.4 denotes the conditions for G_{max} = 100 G/cm and TE = 40 ms, as might be possible for imaging a mouse on a small animal MRI system. In the low gradient frequency range (< 300 Hz), sufficiently large b values can be obtained so that ΔS is primarily dependent on ADC differences. The ADC difference increases with gradient frequency (see Fig. 5-2), so ΔS also increases with gradient frequency. However, in the higher gradient frequency range (> 300 Hz), ΔS decreases with frequency because b_{max} is proportional to $1/f^2$. The peak of ΔS appears at around 300 Hz when the maximum practical contrast is obtained in OGSE measurements with these conditions. Note that the peak contrast occurs well below the frequency where the ADC differences level out (Fig. 5-2), which means that with larger gradient amplitudes, even greater

contrast between tissue I and II would be attainable from OGSE.

Likewise, with smaller gradient amplitudes, the advantages of the OGSE are reduced. The dashed curve demonstrates a lesser but still substantial gain in OGSE contrast as compared to PGSE when G_{max} = 40 G/cm and TE = 40 ms, as might be possible for imaging a rat on a small animal MRI system. However, when G_{max} is reduced to 8 G/cm, even with an increase in TE to 80 ms, the dot-dash curve shows that OGSE contrast is not as great as would be obtained by PGSE. Note that the lowest frequency in Fig. 5-4 is 50 Hz because of the echo time limitation (40 ms). If lower frequencies (< 50 Hz) can be achieved in measurements, it can be expected that the contrasts by OGSE method approach those by PGSE method. Notice that Fig.4 shows the contrast, but since noise is not changing with gradient frequency, this is proportional to the CNR, from which the uncertainty in estimated ADC can be calculated.

5.5 Conclusion and Discussion

Measurements of the sizes of cell nuclei have been suggested as useful biomarkers of malignant state and tumor grade. Imaging methods that can distinguish such sub-cellular properties are likely useful in the context of evaluating tumors non-invasively. However, due to hardware limitations, conventional measurements of ADC using the PGSE method are dominated by changes in tumor cell densities and are relatively insensitive to variations in diffusion at sub-cellular length scales. By contrast the OGSE method measures remarkable differences between tissues that differ only in terms of intracellular structure. Hence, ADC measurements with the OGSE method should be useful for probing nuclear size variations. This would enhance the ability of diffusion imaging to be used as a biomarker for assessing the state of tumors. Our simulations show that the OGSE method can provide more contrast and be sensitized to changes that are not detectable by conventional PGSE methods. A preliminary experimental study has been recently reported which investigated C6 gliosarcoma in a rat model with OGSE and PGSE, which confirmed that the OGSE method is more sensitive to structural variations within tumors than the PGSE measurements (84). It should be noted that the actual intracellular structural

changes that take place in cancerous cells are much more complex than the tissue model considered here. For example the nucleus changes dynamically and the diffusion and relaxation properties may vary during cell division and apoptosis. However, the simple model analyzed above was chosen to demonstrate the feasibility of using OGSE to probe intra-cellular structural changes, such as nuclear size variations. Moreover, the lack of available experimental data makes it difficult to more precisely model diffusion changes during cell proliferation and apoptosis. Here, all diffusion coefficients are assumed constant in the present work. These techniques can be readily implemented on current small animal scanners, though their use in humans will be limited using present gradient systems. These simulations provide a useful background for ongoing and future experimental studies.

CHAPTER VI

CONCLUSION AND FUTURE DIRECTION

Diffusion-weighted magnetic resonance imaging (DWI) provides unique insights for probing biological tissue microstructure and is an important tool in clinical practice and research. Usually, conventional DWI measurements employ a pulsed gradient spin echo (PGSE) method, which uses two identical diffusion-sensitizing gradients on each side of a refocusing RF pulse. The PGSE method has been widely used in conventional DWI measurements which have achieved great successes clinically and in research, such as for stroke diagnosis and detection of cancer. Conventional ADC measurements on MRI systems use the pulsed gradient spin echo (PGSE) method, in which gradients are applied in pairs, separated by a diffusion interval. Because of hardware limitations, and in order to impart sufficient diffusion weighting to be able to see significant signal reductions, the diffusion intervals used in practice are relatively long. Hence, conventional DWI measurements actually represent the integrated effects of obstructions to free diffusion at all scales up to the limiting value determined by the experimentally-selected diffusion interval and they cannot distinguish these from restrictions that occur at smaller scales, such as those associated with intracellular structures. However, it has been reported that intra-cellular structures may be useful in cancer detecting or tumor grading. The Oscillating gradient spin echo (OGSE) method, which replaces the diffusion-sensitizing gradients by a cosine-modulated (or sine-modulated) gradients, has the ability to reduce diffusion times in order to probe short length scales and has great potential in cancer MR imaging. In this dissertation, diffusion temporal spectroscopy has been comprehensively studied, including the background theory, computer simulation, tissue modeling, DWI experiments and applications. The original major contributions of this thesis include:

(1). Improving the conventional finite difference method for computer simulations. By introducing a revised periodic boundary condition (RPBC) to remove the edge effect artifacts arise from the artificial boundaries and developing a tightly-coupled parallel computing

model, the improved finite difference method can be used to study any kind of diffusion methods, including both PGSE and OGSE, more accurately and efficiently.

(2). Modeling of biological tissues and DWI signals with diffusion temporal spectroscopy. It is difficult to model the DWI signals with OGSE method because OGSE has relatively more complicated diffusion-sensitizing gradient waveforms compared with PGSE. Based on the frequency domain analysis method introduced by Stepisnik, analytical expressions for restricted diffusion inside some simple geometries with cosine-modulated OGSE method have been derived in this dissertation. Combined with modeling biological tissues into packed regular geometrical structures, DWI signals obtained with OGSE method can be fitted well and tissue microstructural parameters can be obtained. Such modeling provides a framework to interpret experimental DWI data with OGSE and a powerful tool for probing biological tissue microstructural parameters, such as cell or axon sizes.

(3). Discovering the increase of sensitivity of DWI measurements to variations of intracellular structures, such as nuclear sizes, by OGSE method. PGSE method is insensitive to intracellular structures while OGSE method has been shown in this thesis that it has the ability to probe nuclear size changes. This feature of OGSE would enhance the ability of diffusion imaging to be used as a biomarker for assessing the state of tumors.

The water exchange rate is not considered in the current work. However, it has been shown that water exchange rate might play an important role in DWI measurements (85,86). Karger *et al.* introduced a model to include water exchange rates in the DWI signals (87) and makes it possible to obtain cell membrane permeability and water molecule lifetime in intra- and extra-cellular space. Such a model has been implemented with PGSE method in several works (85,88-90). It would be a future direction to include water exchange into our model with diffusion temporal spectroscopy. Currently, the application of OGSE is limited by the gradient strength so that the applied gradient frequency usually cannot exceed several kilohertz, corresponding to a diffusion length scale less than several microns. With the application of diffusion gradient coils with much higher maximum amplitudes and much faster slew rate, it is possible to push the maximum

gradient frequency up to tens of kilohertz, which corresponds to diffusion length scales less than a micron, making it possible to probe inside the nuclear structure and provide addition contrast in DWI that cannot be detectable by conventional PGSE and OGSE with low frequencies.

REFERENCES

1. Rabi II, Zacharias JR, Millman S, Kusch P. A New Method of Measuring Nuclear Magnetic Moment. Physical Review 1938;53(4):318.
2. Purcell EM, Torrey HC, Pound RV. Resonance Absorption by Nuclear Magnetic Moments in a Solid. Physical Review 1946;69(1-2):37.
3. Bloch F, Hansen WW, Packard M. Nuclear Induction. Physical Review 1946;69(3-4):127.
4. Hahn EL. Spin Echoes. Physical Review 1950;80(4):580.
5. Lauterbu.Pc. Image Formation by Induced Local Interactions - Examples Employing Nuclear Magnetic-Resonance. Nature 1973;242(5394):190-191.
6. Wehrli FW. On the 2003 Nobel Prize in medicine or physiology awarded to Paul C. Lauterbur and Sir Peter Mansfield. Magn Reson Med 2004;51(1):1-3.
7. Mansfield P. Multi-Planar Image-Formation Using Nmr Spin Echoes. Journal of Physics C-Solid State Physics 1977;10(3):L55-L58.
8. Damadian R. Tumor Detection by Nuclear Magnetic Resonance. Science 1971;171(3976):1151-&.
9. Ogawa S, Lee TM, Kay AR, Tank DW. Brain magnetic resonance imaging with contrast dependent on blood oxygenation. Proc Natl Acad Sci U S A 1990;87(24):9868-9872.
10. Moseley ME, Kucharczyk J, Mintorovitch J, Cohen Y, Kurhanewicz J, Derugin N, Asgari H, Norman D. Diffusion-weighted MR imaging of acute stroke: correlation with T2-weighted and magnetic susceptibility-enhanced MR imaging in cats. AJNR Am J Neuroradiol 1990;11(3):423-429.
11. Tuch DS, Harvard University--MIT Division of Health Sciences and Technology. Diffusion MRI of complex tissue structure [Thesis Ph. D. --Harvard--Massachusetts Institute of Technology Division of Health Sciences and Technology 2002.]; 2002. 220 p.
12. Carr HY, Purcell EM. Effects of Diffusion on Free Precession in Nuclear Magnetic Resonance Experiments. Physical Review 1954;94(3):630.

13. Torrey HC. Bloch Equations with Diffusion Terms. Physical Review 1956;104(3):563.

14. Stejskal EO, Tanner JE. Spin Diffusion Measurements - Spin Echoes in Presence of a Time-Dependent Field Gradient. Journal of Chemical Physics 1965;42(1):288.

15. Cory DG, Garroway AN. Measurement of translational displacement probabilities by NMR: an indicator of compartmentation. Magn Reson Med 1990;14(3):435-444.

16. Callaghan PT, Coy A, Macgowan D, Packer KJ, Zelaya FO. Diffraction-Like Effects in Nmr Diffusion Studies of Fluids in Porous Solids. Nature 1991;351(6326):467-469.

17. Basser PJ, Mattiello J, LeBihan D. Estimation of the effective self-diffusion tensor from the NMR spin echo. J Magn Reson B 1994;103(3):247-254.

18. Basser PJ, Mattiello J, LeBihan D. MR diffusion tensor spectroscopy and imaging. Biophys J 1994;66(1):259-267.

19. Mori S, Crain BJ, Chacko VP, van Zijl PC. Three-dimensional tracking of axonal projections in the brain by magnetic resonance imaging. Ann Neurol 1999;45(2):265-269.

20. Taylor DG, Bushell MC. The spatial mapping of translational diffusion coefficients by the NMR imaging technique. Phys Med Biol 1985;30(4):345-349.

21. Le Bihan D, Breton E, Lallemand D, Grenier P, Cabanis E, Laval-Jeantet M. MR imaging of intravoxel incoherent motions: application to diffusion and perfusion in neurologic disorders. Radiology 1986;161(2):401-407.

22. Le Bihan D, Breton E, Lallemand D, Aubin ML, Vignaud J, Laval-Jeantet M. Separation of diffusion and perfusion in intravoxel incoherent motion MR imaging. Radiology 1988;168(2):497-505.

23. Zhao M, Pipe JG, Bonnett J, Evelhoch JL. Early detection of treatment response by diffusion-weighted 1H-NMR spectroscopy in a murine tumour in vivo. Br J Cancer 1996;73(1):61-64.

24. Chenevert TL, McKeever PE, Ross BD. Monitoring early response of experimental brain tumors to therapy using diffusion magnetic resonance imaging. Clin Cancer Res 1997;3(9):1457-1466.

25. Haacke EM. Magnetic resonance imaging : physical principles and sequence design. New York: Wiley; 1999. xxvii, 914 p.
26. Stejskal EO. Use of Spin Echoes in a Pulsed Magnetic-Field Gradient to Study Anisotropic Restricted Diffusion and Flow. Journal of Chemical Physics 1965;43(10P1):3597.
27. Callaghan PT. Principles of nuclear magnetic resonance microscopy. Oxford [England] New York: Clarendon Press ; Oxford University Press; 1991. xvii, 492 p.
28. Brownstein KR, Tarr CE. Importance of Classical Diffusion in Nmr-Studies of Water in Biological Cells. Physical Review A 1979;19(6):2446-2453.
29. Balinov B, Jonsson B, Linse P, Soderman O. The Nmr Self-Diffusion Method Applied to Restricted Diffusion - Simulation of Echo Attenuation from Molecules in Spheres and between Planes. Journal of Magnetic Resonance Series A 1993;104(1):17-25.
30. Soderman O, Jonsson B. Restricted Diffusion in Cylindrical Geometry. Journal of Magnetic Resonance Series A 1995;117(1):94-97.
31. Callaghan PT. Pulsed-Gradient Spin-Echo Nmr for Planar, Cylindrical, and Spherical Pores under Conditions of Wall Relaxation. Journal of Magnetic Resonance Series A 1995;113(1):53-59.
32. Stepisnik J. Analysis of Nmr Self-Diffusion Measurements by a Density-Matrix Calculation. Physica B & C 1981;104(3):350-364.
33. Callaghan PT, Stepisnik J. Frequency-Domain Analysis of Spin Motion Using Modulated-Gradient Nmr. Journal of Magnetic Resonance Series A 1995;117(1):118-122.
34. Parsons EC, Jr., Does MD, Gore JC. Temporal diffusion spectroscopy: theory and implementation in restricted systems using oscillating gradients. Magn Reson Med 2006;55(1):75-84.
35. Gross B, Kosfeld R. Anwendung der spin-echo-methode der messung der selbstdiffusion. Messtechnik 1969;77:171-177.
36. Stepisnik J. Time-Dependent Self-Diffusion by Nmr Spin-Echo. Physica B

1993;183(4):343-350.

37. Does MD, Parsons EC, Gore JC. Oscillating gradient measurements of water diffusion in normal and globally ischemic rat brain. Magnetic Resonance in Medicine 2003;49(2):206-215.

38. Szafer A, Zhong J, Gore JC. Theoretical model for water diffusion in tissues. Magn Reson Med 1995;33(5):697-712.

39. Hwang SN, Chin CL, Wehrli FW, Hackney DB. An image-based finite difference model for simulating restricted diffusion. Magn Reson Med 2003;50(2):373-382.

40. Chin CL, Wehrli FW, Hwang SN, Takahashi M, Hackney DB. Biexponential diffusion attenuation in the rat spinal cord: computer simulations based on anatomic images of axonal architecture. Magn Reson Med 2002;47(3):455-460.

41. Fletcher CAJ. Computational techniques for fluid dynamics. Berlin ; New York: Springer-Verlag; 1988. v. p.

42. Xu JZ, Does MD, Gore JC. Simulating Water Diffusion in Tissues with an Improved Finite Difference Method. 2006; Seattle, USA. p 708.

43. Callaghan PT. A simple matrix formalism for spin echo analysis of restricted diffusion under generalized gradient waveforms. J Magn Reson 1997;129(1):74-84.

44. Sukstanskii AL, Yablonskiy DA. Effects of restricted diffusion on MR signal formation. Journal of Magnetic Resonance 2002;157(1):92-105.

45. Beaulieu C, Allen PS. Determinants of Anisotropic Water Diffusion in Nerves. Magnetic Resonance in Medicine 1994;31(4):394-400.

46. Tu SJ, Shaw CC, Chen L. Noise simulation in cone beam CT imaging with parallel computing. Phys Med Biol 2006;51(5):1283-1297.

47. Quinn MJ. Parallel programming in C with MPI and OpenMP. Boston: McGraw-Hill Higher Education; 2004. xiv, 529 p.

48. Xu J, Does MD, Gore JC. Numerical study of water diffusion in biological tissues using an improved finite difference method. Phys Med Biol 2007;52(7):N111-126.

49. Schachter M, Does MD, Anderson AW, Gore JC. Measurements of restricted diffusion using an oscillating gradient spin-echo sequence. Journal of Magnetic Resonance 2000;147(2):232-237.

50. Perrins WT, Mckenzie DR, Mcphedran RC. Transport-Properties of Regular Arrays of Cylinders. Proceedings of the Royal Society of London Series a-Mathematical Physical and Engineering Sciences 1979;369(1737):207-225.

51. Warach S, Chien D, Li W, Ronthal M, Edelman RR. Fast magnetic resonance diffusion-weighted imaging of acute human stroke. Neurology 1992;42(9):1717-1723.

52. Anderson AW, Xie J, Pizzonia J, Bronen RA, Spencer DD, Gore JC. Effects of cell volume fraction changes on apparent diffusion in human cells. Magn Reson Imaging 2000;18(6):689-695.

53. Arai Y, Okubo K, Terada N, Matsuta Y, Egawa S, Kuwao S, Ogura K. Volume-weighted mean nuclear volume predicts tumor biology of clinically organ-confined prostate cancer. Prostate 2001;46(2):134-141.

54. Hsu CY, Kurman RJ, Vang R, Wang TL, Baak J, Shih Ie M. Nuclear size distinguishes low- from high-grade ovarian serous carcinoma and predicts outcome. Hum Pathol 2005;36(10):1049-1054.

55. Assaf Y, Freidlin RZ, Rohde GK, Basser PJ. New modeling and experimental framework to characterize hindered and restricted water diffusion in brain white matter. Magn Reson Med 2004;52(5):965-978.

56. Assaf Y, Blumenfeld-Katzir T, Yovel Y, Basser PJ. AxCaliber: a method for measuring axon diameter distribution from diffusion MRI. Magn Reson Med 2008;59(6):1347-1354.

57. Van Zijl PC, Moonen CT, Faustino P, Pekar J, Kaplan O, Cohen JS. Complete separation of intracellular and extracellular information in NMR spectra of perfused cells by diffusion-weighted spectroscopy. Proc Natl Acad Sci U S A 1991;88(8):3228-3232.

58. Assaf Y, Cohen Y. In vivo and in vitro bi-exponential diffusion of N-acetyl aspartate (NAA) in rat brain: a potential structural probe? NMR Biomed 1998;11(2):67-74.

59. Mulkern RV, Gudbjartsson H, Westin CF, Zengingonul HP, Gartner W, Guttmann CR, Robertson RL, Kyriakos W, Schwartz R, Holtzman D, Jolesz FA, Maier SE. Multi-component apparent diffusion coefficients in human brain. NMR Biomed 1999;12(1):51-62.

60. Maier SE, Bogner P, Bajzik G, Mamata H, Mamata Y, Repa I, Jolesz FA, Mulkern RV. Normal brain and brain tumor: multicomponent apparent diffusion coefficient line scan imaging. Radiology 2001;219(3):842-849.

61. Mulkern RV, Vajapeyam S, Robertson RL, Caruso PA, Rivkin MJ, Maier SE. Biexponential apparent diffusion coefficient parametrization in adult vs newborn brain. Magn Reson Imaging 2001;19(5):659-668.

62. Brugieres P, Thomas P, Maraval A, Hosseini H, Combes C, Chafiq A, Ruel L, Breil S, Peschanski M, Gaston A. Water diffusion compartmentation at high b values in ischemic human brain. AJNR Am J Neuroradiol 2004;25(5):692-698.

63. Koh DM, Takahara T, Imai Y, Collins DJ. Practical Aspects of Assessing Tumors Using Clinical Diffusion-weighted Imaging in the Body. Magn Reson Med Sci 2008;6(4):211-224.

64. Li JG, Stanisz GJ, Henkelman RM. Integrated analysis of diffusion and relaxation of water in blood. Magn Reson Med 1998;40(1):79-88.

65. Stanisz GJ, Henkelman RM. Diffusional anisotropy of T2 components in bovine optic nerve. Magn Reson Med 1998;40(3):405-410.

66. Reuben H. Fan MDD. Compartmental relaxation and diffusion tensor imaging measurements <I>in vivo</I> in lambda-carrageenan-induced edema in rat skeletal muscle. NMR in Biomedicine 2008;21(6):566-573.

67. Niendorf T, Dijkhuizen RM, Norris DG, van Lookeren Campagne M, Nicolay K. Biexponential diffusion attenuation in various states of brain tissue: implications for diffusion-weighted imaging. Magn Reson Med 1996;36(6):847-857.

68. Mulkern RV, Zengingonul HP, Robertson RL, Bogner P, Zou KH, Gudbjartsson H,

Guttmann CR, Holtzman D, Kyriakos W, Jolesz FA, Maier SE. Multi-component apparent diffusion coefficients in human brain: relationship to spin-lattice relaxation. Magn Reson Med 2000;44(2):292-300.

69. Clark CA, Le Bihan D. Water diffusion compartmentation and anisotropy at high b values in the human brain. Magn Reson Med 2000;44(6):852-859.

70. Sehy JV, Ackerman JJ, Neil JJ. Evidence that both fast and slow water ADC components arise from intracellular space. Magn Reson Med 2002;48(5):765-770.

71. Grant SC, Buckley DL, Gibbs S, Webb AG, Blackband SJ. MR microscopy of multicomponent diffusion in single neurons. Magn Reson Med 2001;46(6):1107-1112.

72. Schwarcz A, Bogner P, Meric P, Correze JL, Berente Z, Pal J, Gallyas F, Doczi T, Gillet B, Beloeil JC. The existence of biexponential signal decay in magnetic resonance diffusion-weighted imaging appears to be independent of compartmentalization. Magn Reson Med 2004;51(2):278-285.

73. Sukstanskii AL, Ackerman JJH, Yablonskiy DA. Effects of barrier-induced nuclear spin magnetization inhomogeneities on diffusion-attenuated MR signal. Magnetic Resonance in Medicine 2003;50(4):735-742.

74. Kiselev VG, Il'yasov KA. Is the "biexponential diffusion" biexponential? Magn Reson Med 2007;57(3):464-469.

75. Zhong JH, Gore JC. Studies of restricted diffusion in heterogeneous media containing variations in susceptibility. Magn Reson Med 1991;19(2):276-284.

76. Thelwall PE, Grant SC, Stanisz GJ, Blackband SJ. Human erythrocyte ghosts: exploring the origins of multiexponential water diffusion in a model biological tissue with magnetic resonance. Magn Reson Med 2002;48(4):649-657.

77. Fang SC, de los Reyes C, Umen JG. Cell size checkpoint control by the retinoblastoma tumor suppressor pathway. PLoS Genet 2006;2(10):e167.

78. Deman JJ, Bruyneel EA. Thermal transitions in the adhesiveness of HeLa cells: effects of cell growth, trypsin treatment and calcium. J Cell Sci 1977;27:167-181.

79. Sugahara T, Korogi Y, Kochi M, Ikushima I, Shigematu Y, Hirai T, Okuda T, Liang L, Ge Y, Komohara Y, Ushio Y, Takahashi M. Usefulness of diffusion-weighted MRI with echo-planar technique in the evaluation of cellularity in gliomas. J Magn Reson Imaging 1999;9(1):53-60.

80. Gauvain KM, McKinstry RC, Mukherjee P, Perry A, Neil JJ, Kaufman BA, Hayashi RJ. Evaluating pediatric brain tumor cellularity with diffusion-tensor imaging. AJR Am J Roentgenol 2001;177(2):449-454.

81. Guo Y, Cai YQ, Cai ZL, Gao YG, An NY, Ma L, Mahankali S, Gao JH. Differentiation of clinically benign and malignant breast lesions using diffusion-weighted imaging. J Magn Reson Imaging 2002;16(2):172-178.

82. Lyng H, Haraldseth O, Rofstad EK. Measurement of cell density and necrotic fraction in human melanoma xenografts by diffusion weighted magnetic resonance imaging. Magn Reson Med 2000;43(6):828-836.

83. Zink D, Fischer AH, Nickerson JA. Nuclear structure in cancer cells. Nat Rev Cancer 2004;4(9):677-687.

84. Colvin DC, Yankeelov TE, Does MD, Yue Z, Quarles C, Gore JC. New insights into tumor microstructure using temporal diffusion spectroscopy. Cancer Res 2008;68(14):5941-5947.

85. Meier C, Dreher W, Leibfritz D. Diffusion in compartmental systems. I. A comparison of an analytical model with simulations. Magn Reson Med 2003;50(3):500-509.

86. Meier C, Dreher W, Leibfritz D. Diffusion in compartmental systems. II. Diffusion-weighted measurements of rat brain tissue in vivo and postmortem at very large b-values. Magn Reson Med 2003;50(3):510-514.

87. Karger J, Pfeifer H, Heink W. Principles and Application of Self-Diffusion Measurements by Nuclear Magnetic Resonance. Adv Magn Reson 1988;12:1-89.

88. Stanisz GJ, Szafer A, Wright GA, Henkelman RM. An analytical model of restricted diffusion in bovine optic nerve. Magn Reson Med 1997;37(1):103-111.

89. Nilsson M, Latt J, Nordh E, Wirestam R, Stahlberg F, Brockstedt S. On the effects of a varied diffusion time in vivo: is the diffusion in white matter restricted? Magn Reson Imaging 2008.

90. Roth Y, Ocherashvilli A, Daniels D, Ruiz-Cabello J, Maier SE, Orenstein A, Mardor Y. Quantification of water compartmentation in cell suspensions by diffusion-weighted and T(2)-weighted MRI. Magn Reson Imaging 2008;26(1):88-102.